Structure of pre-monsoon convective systems over a tropical coastal region in southwest India using C-band polarimetric doppler weather radar observations

Dharmadas Jash[1,2], Resmi E.A[1], Unnikrishnan C.K[1], Sumesh R.K[1], Nita Sukumar[1], Sumit Kumar[1,2]

[1]National Centre for Earth Science Studies (NCESS), P.B. No. 7250 Akkulam, Thiruvananthapuram, Kerala, India - 695011.

[2]Department of Atmospheric Sciences, Cochin University of Science and Technology (CUSAT), Ernakulam, Kerala, India - 682022

Key points:

- Structure of pre-monsoon convective systems has been revealed using polarimetric radar and other supporting instruments.
- Reflectivity values greater than 30 dBZ reaching up to 10 km height has been observed in the rapid development stage of thunderstorms.
- Graupels along the high reflectivity columns inside the storms suggest presence of strong updraft.
- Existence of vertical ice particles indicate strong electric field inside thunderstorms.

[*]*Corresponding author address*: E. A. Resmi, National Centre for Earth Science Studies (NCESS), Thiruvananthapuram, India; E-mail: resmi.ea@ncess.gov.in

Abstract: The structure of pre-monsoon convective systems over southern peninsular India using polarimetric doppler weather radar (DWR) observations has been analyzed. Convective-stratiform separation has been done for eleven convective events during Mar-May, 2018. The mean vertical profile of reflectivity shows peak reflectivity of 32 dBZ near 3 km height for convective regions and the bright band signature over stratiform regions was observed. The frequency distributions of reflectivity at 3 km height over convective and stratiform regions are of bell-shaped nature with peaks at 32 dBZ and 18 dBZ respectively. A comprehensive analysis has been done on two prominent convective cases on 13th and 25th May 2018. Strong convective regions represented by high reflectivity (> 45 dBZ) were noticed in the PPI diagrams. Specific differential phase (K_{dp}) has been calculated from the slope of the filtered Φ_{dp}. Heavy precipitation near surface is reflected in the high value of K_{dp} (> 5° km^{-1}). High values of Z_{dr} (> 3 dB) were measured at lower levels due to the oblate bigger raindrops. A fuzzy logic-based hydrometeor identification algorithm has been applied with five variables (Z_h, Z_{dr}, ρ_{hv}, $K_{dp,}$ and T) to understand the bulk microphysical processes at different heights within convective regions. The presence of bigger graupel particles near the melting layer indicates strong updrafts within the convective core regions. The vertical ice hydrometeor might signify the existence of a strong electric field causing them to align vertically and this could be linked to lightning occurrence associated with such systems.

Keywords: Pre-monsoon, Convective systems, Doppler weather radar, Hydrometeor identification

1. Introduction

Thunderstorms are severe mesoscale weather phenomena that develop mainly due to intense convection over the heated landmass and are accompanied by heavy rainfall, lightning, and sometimes hail. They have a spatial extent of a few kilometres to few hundred kilometres and a life span of less than an hour to several hours (Tyagi et al., 2012; Saha et al., 2014; Thakur et al 2019). Numerous thunderstorms occur daily across the globe (Christian et al., 2003), a major fraction of which is over the tropical belt. In the case of Indian subcontinent, most of the thunderstorms occur during the pre-monsoon (March-April-May) season (Singh & Bhardwaj, 2019). They are locally known as *Kalbaisakhi* in West Bengal, *Bordoichila* in Assam and *Andhi* in north-west India. A large amount of precipitation particularly during the pre-monsoon season occur due to thunderstorm events (Saha et al., 2014; Bhardwaj & Singh, 2018). Using satellite data, Cecil et al. (2014) has prepared lightning climatology across the globe, which clearly shows different hotspots, especially over the tropical region. Halder and Mukhopadhyay (2016) have identified five lightning hotpots during pre-monsoon and one among them is over the southern peninsular India. Using data from different observatories across India, Tyagi (2007) has shown that, the highest annual thunderstorm frequency is observed over Assam and sub-Himalayan West Bengal in the east, Jammu region in the north and over Kerala, where the frequency of thunderstorm is higher, in the southern peninsula. Manohar and Kesarkar (2004) have shown that thunderstorm frequency peaks in the month of May over southern India. Study by Unnikrishnan et al. (2021) on lightning activity using TRMM-LIS data and ground-based lightning detection network shows strong lightning activity over south India particularly over the Kerala region. Effect of orography, along with abundant supply of moisture from the sea and presence of land-sea breeze are some of the important factors that favour the occurrence of thunderstorms over the southwest peninsular region (Rao & Srinivasan, 1969; Romatschke et al., 2011).

Thunderstorms cause damage to crops, properties and even human lives every year. It is estimated that between 1500 and 2800 deaths occurred annually due to thunderstorms/lightning during 2001-2017 (Roy et al., 2019). Heavy rainfall and high winds from these weather systems cause an interruption in connectivity among different places and infrastructure in general. Hence, there is an increasing demand for better nowcasting of such weather systems. Several attempts have been made to predict such systems using statistical approach (Ravi et al., 1999; Dhawan et al., 2008; Rajeevan et al., 2012), satellite-based nowcasting (Purdom 2003; Umakanth et al., 2021), numerical

simulations (Abhilash et al., 2007; Litta & Mohanty 2008; Rajeevan et al., 2010; Litta et al., 2012; Madhulatha & rajeevan 2018; Leena et al 2019; Sad et al., 2021) and even artificial intelligence (Elio et al., 1987; Litta et al., 2013; Zhou et al., 2019). But because of their small-scale nature and innate underlying nonlinearity, prediction of such systems is far from desirable accuracy. More observations are required to understand the features and internal structures of these systems which in turn will help their forecasting. Most of the thunderstorm related studies in India were on pre-monsoon thunderstorms (Nor'westers) occurring over east and north-east parts of India (Litta & Mohanty, 2008; Mukhopadhyay et al., 2009; Tyagi et al., 2012; Thakur et al., 2019). A few studies (Rajeevan et al., 2010; Suresh 2012; Agnihotri et al., 2020) have been conducted on the thunderstorm occurrences over the southern peninsular India, particularly over Kerala which is one of the potential lightning hotspots in the southern peninsular India. Proximity of the Arabian Sea backed by the towering Western Ghats orography influences the formation and development of clouds and thunderstorms in the region.

Doppler weather radar (DWR) is one of the most relevant and reliable instrument to monitor these weather events in 3-dimension, starting from their genesis to dissipating stage. Radars have been used in numerous studies (Mukhopadhyay et al., 2009; Rajeevan et al., 2010; Srivastava et al., 2010; Litta et al., 2012; Suresh 2012) to understand the structure and evolution of thunderstorms. But most of these studies mainly use radar reflectivity and sometimes radial velocity also. However, studies using polarimetric radars are rare particularly over the Indian region mainly because of less availability of such data. Radars with polarimetric capabilities could provide much more information about the precipitating systems e.g., about size and shape of the hydrometeors within the system.

Polarimetry has two major advantages viz. polarimetric measurements improve the retrieval of microphysical parameters such as mean drop size, rainfall estimation (Chandrasekar et al., 1990; Bringi et al., 2006; Bringi et al., 2009; Cifelli et al., 2011) and polarimetric clutter-detection techniques help in the removal of non-meteorological echoes (Zrnic´ & Ryzhkov, 1999; Unal, 2009; Islam et al., 2012; Lakshmanan et al., 2014). Since polarimetric measurements contain information on the shape and size of the hydrometeors, they can be used for better retrieval of hydrometeor types. Fuzzy-logic based hydrometeor identification (HID) is a very efficient and popular method for identifying hydrometeors within the radar scan volume (Vivekanandan et al., 1999; Liu & Chandrasekar, 2000; Keenan, 2003; Marzano et al., 2006; Dolan & Rutledge, 2009; Dolan et al., 2013). Such studies give valuable information about different ice hydrometeors present at different

heights within a precipitating system. Unlike raindrops, it is not easy to obtain information about ice particles using remote sensing techniques, mainly because of their irregular shapes and varying densities. Hydrometeor identification algorithms provide an indirect way to obtain information on ice particles. Such information can help us understand the charge separation and subsequent lightning in thunderstorms as detailed in different laboratory studies (Takahashi, 1978; Jayaratne et al., 1983; Saunders et al., 1991). These studies suggest that the non-inductive charge separation due to rebounding collision between graupel and ice crystals in the presence of super-cooled water droplets is the main mechanism of thunderstorm charging. Hence hydrometeor identification is particularly important during thunderstorm events. Subrahmanyam and Baby (2020) studied the spatial structure of the Ockhi cyclone and implemented HID algorithm using polarimetric doppler weather radar observations at the west coast of southern peninsular India and provided information about polarimetric signatures of rain-bearing clouds. However, the hydrometeor classification studies are rare over the Indian region, mainly because of the lack of radars with polarimetric capabilities.

C-band polarimetric doppler weather radar data and several other observation data are used in this study to understand the features of pre-monsoon thunderstorms over southern peninsular India. A hydrometeor classification algorithm has been applied to obtain information on hydrometeors. The paper is organized as follows, apart from the introduction (Section 1), the data from different instruments and methodology are described in Section 2. Results and discussions are presented in Section 3. Section 4 summarizes the major findings/conclusions drawn from the study.

2. Data and Methodology

We have identified eleven convective events over the southern peninsular India during the pre-monsoon period (i.e., Mar to May) of 2018 using C-band radar reflectivity field. For these events convective-stratiform separation has been done to obtain statistics on radar reflectivity over convective and stratiform regions. Two prominent convective events on 13th May and 25th May, 2018 have been selected as representative cases for further analysis. Besides the DWR data, we have used rain drop size distribution (DSD) data from disdrometer, cloud base height (CBH; m) data from ceilometer, brightness temperature data from INSAT satellite, ERA5 reanalysis data and also radiosonde measurements. Disdrometer and ceilometer were installed over the rooftop of the National Centre for Earth Science Studies (NCESS; 8.5228N, 76.9097E). Locations of the DWR

and NCESS along with the topography of the surrounding area are shown in Figure 1. A brief description of the instruments and data is summarized in Table 1.

Optical disdrometer (model: OTT Parsivel, manufactured by OTT Hydromet, Germany) is a laser-based system that detects all types of precipitation at the surface (Löffler-Mang and Joss, 2000; Friedrich et al., 2013). It measures rain DSD and fall velocity distribution in 32 size and velocity classes as well as it provides rain rates (R; mm h^{-1}) and radar reflectivity (dBZ). The size of measurable liquid precipitation particles ranges from 0.2 to 8 mm and it varies from 0.2 to 25 mm for solid precipitation particles. It can measure the particles fall velocity from 0.2 to 20 ms^{-1}. The temporal resolution of this data is 1 minute. The disdrometer used in this study was installed over rooftop of NCESS.

Ceilometer (model: CHM15k-Nimbus manufactured by Lufft Mess-und Regeltechnik GmbH) is a ground-based remote sensing device that uses standard lidar method to determine the cloud base height (CBH) from the altitude profile of backscattered signals. It can provide cloud thickness where the cloud layers do not totally attenuate the laser beam. But the signals get attenuated in a rainy situation depending on the number concentration and size of raindrops and hence signal to noise ratio of the ceilometer decreases with increasing rain rate (Clothiaux et al., 2000). Technical details of CHM15k can be obtained from the previous studies by Heese et al. (2010) and Sumesh et al. (2019). The CHM15k is operated with a vertical resolution of 15 m and the CBH is measured with a temporal resolution of 15 s.

Brightness temperature data (Infrared Brightness Temperature, IRBT) has been used as a proxy for the cloud top height. This data is obtained from INSAT-3DR which is a multi-purpose geosynchronous spacecraft and provides data with spatial resolution of 4x4 km and temporal resolution of 30 minutes, of mesoscale phenomena in the visible and infrared (IR) spectral bands (0.55-12.5 μm) over the Indian region. This data is freely available through the https://www.mosdac.gov.in/ server.

The synoptic circulations over the study region were analysed using the geopotential (m^2 s^{-2}), u-wind (m s^{-1}) and v-wind (m s^{-1}) variables from ERA5 reanalysis hourly data having spatial resolution of 0.25°x0.25°. Radiosonde measurements from India Meteorological Department (IMD), Thiruvananthapuram have been utilized to analyse the Convective available potential energy (CAPE;

177 J kg^{-1}), vertical profiles of temperature (K), mixing ratio (g kg^{-1}), wind speed (m s^{-1}) and wind
178 direction (deg).

179 **2.1. DWR data and quality control**

180 C-band polarimetric Doppler Weather Radar (DWR), installed at VSSC, Thiruvananthapuram
181 (8.5374N, 76.8657E, 27 m above mean sea level) operates at a frequency of 5.625 GHz and have a
182 peak transmitting power of 250 kW. The radar performs a volumetric scan of the surrounding
183 atmosphere within a radius of 240 km at 11 elevation angles (0.5°, 1°, 2°, 3°, 4°, 7°, 9°, 12°, 15°,
184 18° and 21°) with an azimuthal and radial resolutions of 1° and 150 m respectively. One full volume
185 scan takes around 15 minutes. The radar provides base products such as reflectivity at horizontal
186 polarization (Z_h), differential reflectivity (Z_{dr}), differential propagation phase (Φ_{dp}), cross-
187 correlation(ρ_{hv}), radial velocity (V_r) and Spectral width(σ). Z_{dr} is the difference between reflectivities
188 (in decibel) at horizontal and vertical polarization, Φ_{dp} is the phase difference between the
189 horizontally and vertically polarized pulses. More information about these variables can be found in
190 Doviak and Zrnic (1993) and also in Bringi and Chandrasekar (2001). A comprehensive detail about
191 the radar is given in Mishra et al. (2020). The validation of the radar data with other instruments
192 showed that the DWR reflectivity agrees quite well with GPM satellite measurements and also the
193 radar retrieved precipitation have a good correlation (0.89) with ground based *in-situ* measurements
194 (Kumar et al., 2020).

195 Received signal by radar is often contaminated by signals reflected from non-meteorological
196 objects such as hills, birds etc., anomalous propagation and also attenuation of the electromagnetic
197 wave by different types of hydrometeors (Ryzhkov & Zrnic, 1998; Friedrich et al., 2006; Unal, 2009;
198 Lakshmanan et al., 2014). Even though the radar signal processor takes into account many factors
199 to give reasonably accurate base products from the return signal, still the data needs certain quality
200 control measures. The use of simple thresholds for different variables can be quite useful in removing
201 unwanted echoes (Ryzhkov & Zrnic, 1998; Lakshmanan et al., 2014). The following quality control
202 measures are considered for this study- (i) pixels with Z_h > 70 dBZ or ρ_{hv}<0.7 are ignored, (ii)
203 topography data from Shuttle Radar Topography Mission (SRTM) (Farr et al., 2007) to remove
204 ground clutter from hills present towards 40 km east of the radar (Figure 1) using the method
205 proposed by Friedrich et al., (2006). Figure 2 shows the radar reflectivity during an event on 13th
206 May, 2018 before quality control (Figure 2a) and after quality control (Figure 2b). The clutter due

to hills is present on the reflectivity field before quality control, which is removed nicely after applying the above-mentioned quality control measures. Other variables (Z_{dr}, Φ_{dp} and ρ_{hv}) were processed similarly.

Table 1. Overview of the instruments and the data used in this study

Data source	Parameters used in the study	Spatial resolution	Temporal resolution
C-band polarimetric Doppler weather radar	Reflectivity at horizontal polarization (dBZ), differential reflectivity (dB), differential propagation phase (deg.), cross-correlation	150 m along radial and 1° along azimuth	~ 15 min
Disdrometer (OTT parsivel)	Rain rate (mm h^{-1}), concentration of precipitation particles in diameter classes 0.2-25 mm (m^{-3} mm^{-1}).	In-situ	1 min
Ceilometer (CHM15k)	Cloud base height (m), cloud cover (oktas), cloud penetration depth (m)	-	15 sec
INSAT-3DR	Brightness temperature (K)	4 x 4 km	30 min
ERA-5	u-wind (m s^{-1}), v-wind (m s^{-1}), geopotential (m^2 s^{-2})	0.25° x 0.25°	1 hour
Radiosonde	Temperature (K), mixing ratio (g kg^{-1}), wind speed (m s^{-1}), wind direction (deg.), CAPE (J kg^{-1}) etc.	-	-

2.2. Convective-Stratiform separation

Several studies have been done for the classification of precipitation into convective and stratiform parts using *in-situ* measurements (Tokay & Short, 1996; Testud et al., 2001; Bringi et al., 2003) and weather radars (Steiner et al., 1995; Williams et al., 1995; Biggerstaff & Listemaa, 2000; Ulbrich & Atlas, 2002; Thurai et al., 2010). Convective and stratiform parts of the cloud systems exhibit significantly different behaviours in terms of dynamics as well as microphysics (Houze, 1997). Vertical air motions within these two portions of a cloud system differ significantly; convective parts are mainly driven by large narrow updrafts (5–10 m s^{-1} or more), while stratiform portions are governed by gentler mesoscale ascents (< 3 m s^{-1}). Thus, microphysical processes responsible for particle growth within the convective and stratiform parts are very different. Particles within convective cores regions mainly grow by riming or accretion (collection of supercooled liquid water droplets onto the ice particle surface), which leads to large/dense hydrometeors, whereas in the

stratiform region vapour deposition and aggregation are dominating processes that lead to smaller and less dense ice hydrometeors (though large aggregates may exist).

The convective-stratiform separation method of Steiner et al. (1995), which is based on the texture of the radar reflectivity field is adopted for the present study and is widely used by the radar community. This method basically checks for two criteria viz. *intensity* or *peakedness* criteria on the horizontal reflectivity field at 3 km height, to identify a grid point (pixel) as a convective center. Any grid point with reflectivity at least 40 dBZ (intensity criteria) or greater than a fluctuating threshold (peakedness criterion) depending on the area-averaged background reflectivity (Z_{bg} calculated within a radius of 11km around the grid point), is considered as a convective center. For each pixel identified as a convective center, all surrounding pixels within a certain radius of influence are also included as convective pixels. This radius of influence is dependent on Z_{bg}. Once all the convective pixels are identified, the rest of the pixels with non-zero reflectivity values are assigned as stratiform pixels.

2.3. Φ_{dp} data processing and K_{dp} calculation

The differential propagation phase (Φ_{dp}) is the phase difference between the horizontal and vertical polarized pulses on traversing through the atmosphere. The differential propagation phase is proportional to the water content along a rain path. Since, most of the hydrometeors in the atmosphere are aligned with their major axis in the horizontal plane and it's a range cumulative parameter, the value of Φ_{dp} increases with propagation path. Now, the unambiguous range of Φ_{dp} usually is 180° in the alternate H/V transmission mode and 360° in the simultaneous H/V transmission mode. Hence, for a long propagation path in rain, Φ_{dp} values can easily exceed the unambiguous range and then the Φ_{dp} will be wrapped/folded which is usually manifested as a sudden jump in the range profiles of Φ_{dp}. This issue with Φ_{dp} is known as phase wrapping/folding (Wang & Chandrasekar, 2009; You et al., 2014). The unfolding of these phases has been done by adding appropriate phase offset (You et al., 2014). So, even after the quality control steps mentioned in the previous section, Φ_{dp} needs this extra processing before it can be used in further analysis. In Figure 3a, such a situation of phase wrapping is observed towards 15 km west of the radar during a convective event. Then the phase are unfolded nicely and the unfolded Φ_{dp} is shown in Figure 3b.

Specific differential phase (K_{dp}) is defined as the slope of range profiles of Φ_{dp} (Seliga & Bringi, 1978; Jameson, 1985; Bringi & Chandrasekar, 2001) and is defined as follows.

$$K_{dp}(r) = \left[\frac{\Phi_{dp}\left(r + \frac{\Delta r}{2}\right) - \Phi_{dp}\left(r - \frac{\Delta r}{2}\right)}{2\Delta r}\right] \quad (1)$$

K_{dp} is an important parameter for meteorological applications as it is closely related to rain intensity. More importantly it's insensitive to signal attenuation during propagation, radar calibration, partial beam blockage and the presence of hail (Aydin et al., 1995; Zrnic & Ryzhkov, 1996). This makes specific differential phase very useful for precipitation estimation at heavy rain intensity or during partial beam blockage. Though the estimation of K_{dp} seems quite simple, it requires further processing of Φ_{dp} range profiles before calculating the slope. Φ_{dp} is known to be a very noisy parameter particularly in regions with low rain rates and the process of differentiation increases this noise even further. To tackle this, we have applied a low-pass butterworth filter (Parks & Burrus, 1987; Proakis & Manolakis, 1988) of order 10 with a cut-off scale of 2 km to reduce the statistical fluctuation but keeping the overall features intact. Similar filters with similar cut-off scales have been used in previous studies (Hubbert et al., 1993; Wang & Chandrasekar, 2009). Figure 4a shows the Φ_{dp} Plan Position Indicator (PPI) at 2° elevation angle during the convective event on 13th May after quality control and unfolding. Then the previously mentioned filter has been applied on this Φ_{dp} and obtained a smoothed Φ_{dp} (Figure 4b). Small scale fluctuations in the Φ_{dp} field are nicely removed in the filtered Φ_{dp}. With this smoothed Φ_{dp} field K_{dp} has been estimated using Equation 1 and is shown in Figure 4c. Another K_{dp} estimate using slope of the linear regression line (Balakrishnan & Zrnic, 1990) has also been calculated. Both the methods gave similar K_{dp} values. K_{dp} field shows high values close to 9° km^{-1} at a distance of 5 to 15 km westward from the radar, indicating presence of heavy precipitation. The blue line in this plot represents the 281° azimuth. Along this direction original Φ_{dp} (dot-dashed blue curve), filtered Φ_{dp} (solid blue curve), estimated K_{dp} (red curves) are shown in Figure 4d. The ranges of K_{dp} values obtained here, agrees quite well with previous studies on convective cases (Wang & Chandrasekar, 2009; Dolan et al., 2013).

2.4. Hydrometeor identification

A hydrometeor identification (HID) algorithm by Dolan et al. (2013) is used to identify types of hydrometeors present at different heights within a convective system. This is a fuzzy logic-based algorithm in which a fuzzy logic score (μ) is calculated (Equation 2) for each hydrometeor type and

the hydrometeor with the highest fuzzy logic score is the most probable hydrometeor type at that grid point within the radar scan volume.

$$\mu_i = \left[\frac{W_{Z_{dr}}\beta_{Z_{dr},i} + W_{K_{dp}}\beta_{K_{dp},i} + W_{\rho_{hv}}\beta_{\rho_{hv},i}}{W_{Z_{dr}} + W_{K_{dp}} + W_{\rho_{hv}}}\right]\beta_{T,i}\,\beta_{Z_h,i} \qquad (2)$$

$$\beta = \frac{1}{1 + \left[\left(\frac{x-m}{a}\right)^2\right]^b} \qquad (3)$$

Where, μ_i is the fuzzy logic score for the i^{th} hydrometeor type. $\beta_{j,i}$ is the membership function for i^{th} hydrometeor types and j^{th} variable (Equation 3). W_j is the weight factor for the j^{th} variable. The values of these membership function parameters and the weights are taken as in Dolan et al. (2013), which are obtained from simulation at C-band. Five variables viz. Z_h, Z_{dr}, K_{dp}, ρ_{hv} and temperature (T) are used to calculate the fuzzy logic score. Seven types of hydrometeors have been considered viz. drizzle (DZ), rain (RN), ice crystals (CR), aggregates (AG), low-density graupel (LDG), high-density graupel (HDG), and vertically oriented ice (VI). Graupels are ice particles with diameter of 2-5 mm, which grow mainly due to riming process i.e., collection of supercooled water droplets onto the surface of ice crystals and subsequent freezing. Temperature for the HID scheme has been obtained from radiosonde measurements by IMD Thiruvananthapuram at 5:30 IST (Indian Standard Time). Radar data interpolated on a 0.5x0.5x0.5 km grid have been used for the HID analysis.

3. Results and discussions

3.1. Reflectivity statistics over convective and stratiform regions

An implementation of the convective-stratiform separation algorithm is depicted in Figure 5 during the convective event on 13th May, 2018. Figure 5a shows the reflectivity field averaged between 2.5 and 3.5 km height. Convective-stratiform separation algorithm is then applied on this horizontal reflectivity field and the results are shown in Figure 5b. The red and blue pixels are identified as convective and stratiform precipitation respectively. Not only high reflectivity regions, but also other regions with strong gradient have been identified as convective regions. The convective-stratiform separation has been implemented for all the volume scans available for all the eleven convective

events during Mar-May, 2018 and the corresponding reflectivity statistics are shown in Figure 6. Figure 6(a, b) shows the contour frequency by altitude diagram (CFAD) of the reflectivity over the convective and stratiform regions. The convective core is visible near 3 km height though such feature is not visible in case of stratiform. Figure 6c shows the mean vertical profile of reflectivity over the convective and stratiform regions. For the convective case (red), mean reflectivity gradually increases with height from ground level and reaches a maxima near 3 km height and then gradually decreases with height. Similar features in the reflectivity profile were found over the tropical region by Zipser and Lutz (1994). The peak value of the reflectivity is about 32 dBZ. On the other hand, in stratiform case mean reflectivity remains almost uniform up to 4 km height and it peaks near 5 km height and then gradually decreases with height. This peak in the reflectivity signifies the bright band (caused by enhanced reflectivity from melting ice particles near 0 °C level) over stratiform regions. Figure 6d shows the frequency distribution of reflectivity at 3 km height. The peak of the distributions over the convective (red) and stratiform (blue) regions are well separated though there is an overlap between the two distributions. The dashed vertical line represents the reflectivity corresponding to the rain rate of 10 mm h^{-1}. Here we have used $Z=168R^{1.4}$ relation, which was obtained from another study by Jash et al. (2019) over this region using micro rain radar data. This result clearly shows that use of a rain rate threshold (e.g., 10 mm h^{-1}) to separate convective and stratiform rain is questionable, though such simple classification method is often useful in many studies (Testud et al. 2001; Bringi et al. 2003; Sisodiya et al. 2020).

3.2. Evolution of convective systems

An in-depth analysis is performed on two prominent convective events on 13th May and 25th May, 2018 for the understanding of the evolution and structure of pre-monsoon convective systems over southern peninsula.

3.2.1 An overview of the synoptic conditions

Favourable synoptic and thermodynamic conditions help in the organization of convective storms to develop into severe ones (Mukhopadhyay et al., 2009). High moisture, atmospheric instability, vertical wind shear and a lifting mechanism are the different necessary conditions for the development of thunderstorms. Hence, an overview of the synoptic conditions before and during the events will give more insights into their development. Geopotential height anomaly and wind data from ECMWF Reanalysis v5 (ERA5) at 12 UTC and vertical profile of equivalent potential

temperature (θ_e), mixing ratio, wind speed, wind direction from radiosonde measurements by IMD, Thiruvananthapuram at 00 UTC and 12 UTC were used to look into the environmental conditions for the events.

A low-pressure area formed in the south west Arabian Sea (Figure 7a) on 13th May, 2018 which was evident from the minimum geopotential height anomaly at 700 hPa levels between 55-65E and 4-10N, was far from the study region. Under this influence, the mean wind was from Bay of Bengal to the Arabian Sea in the easterly direction (figure 7a). The strong negative gradient of the θ_e profile up to 3 km height shows the instability in the lower atmosphere (Figure 7c). The mixing ratio profiles indicate the presence of moist layers between 2-6 km levels, also suggest the existence of favourable atmospheric conditions for the formation of thunderstorm. Wind direction changed abruptly along the vertical which is due to the turbulence associated with the unstable lower atmosphere. Heavy rainfall in isolated places were reported over Kerala and Tamil Nadu by IMD. These conditions lead to the formation of convective system over inland region on 13 May 2018 in the afternoon hours between 16:00-22:30 IST.

The convective event occurred over southern peninsula on 25th May 2018, between 13:00-19:00 IST. The lower geopotential height anomaly at 700 hPa level clearly demonstrates the convection is active and strong (Figure 7b) evident with scattered low and medium clouds favouring the intense to very intense convection. The sounding analysis over the study region indicates that, θ_e and mixing profiles in the morning and evening hours shows unstable and moist layers in the near surface levels. Also, the near surface wind was more than 10 ms^{-1} from the south westerly directions (near to monsoon onset). Further to the west, cyclonic vortex Meknu (T5.0) was formed over west central adjoining south west Arabian sea with lay centred over 15.2°N and 54.3°E.

3.2.2 Convective event on 13th May, 2018

Development of the convective system on 13th May 2018 (16:00-22:30 IST) is captured in the plan position indicator (PPI) diagrams of radar reflectivity field at consecutive times during the event (Figure 8). The convective clouds started developing over the land around 25 km east of the radar location at 16:00 IST and then gradually it started moving westward. This movement of the system was due to the prevailing easterly wind (Figure 7a). The cloud system passed over NCESS location around 18:00 IST (Figure 8d). As soon as it reached over the NCESS location extremely heavy rainfall started, which was observed in the rain rate measured by disdrometer (Figure 9a). The rain

rate crossed 100 mm h^{-1} and sustained in that range for over an hour. Gradually the rain intensity declined to a range of 0.1 - 1 mm h^{-1}, which was basically the stratiform precipitation following the main convective activity. The rain DSD obtained by the disdrometer shows an abundance of bigger raindrops (diameter > 3 mm) during this intense convective spell followed by smaller drops at the later stage of the event. The deep convective cloud system eventually moved over the Arabian Sea around 30 km westward from the radar location and meanwhile it turned into a stratiform system (Figure 8g-8i). The IMD weather report also mentioned about the rainfall during these hours. This event was associated with rapid development of deep convective clouds as observed in the evolution of the cloud top infrared brightness temperature (IRBT) measured from satellite (INSAT-3DR). A lower brightness temperature signifies a higher cloud top height. Figure 10a-10e shows the spatial and temporal evolution of the brightness temperature during this event. Around 18:00 IST much of the region was having brightness temperature below 200 K revealing the occurrence of deep clouds over most of the region. Figure 11 (red curve) shows the temporal evolution of the brightness temperature over the NCESS location (averaged over a 12x12 km area centered at NCESS). A rapid decrease in the brightness temperature started at 15:45 IST and reached a minimum value of 185 K at 17:45 IST, which demonstrates how fast such a deep system can develop within such a short span of time. Also, cloud base height measured by ceilometer shows (Figure 12a) the presence of multilevel clouds. Before 17:00 IST mostly high-level clouds are detected (CBH ~ 7 km) and then just before the precipitation starts all three cloud layers are having cloud base below 2.5 km. Such a low cloud base height and high cloud top height (inferred from low IRBT values) measures the depth of the cloud system. Once the rain rate reduced it detected multilevel clouds. The CAPE value of 1713 J kg^{-1} was observed from the nearest radiosonde measurements in the mooring hour (05:30 IST) which was indicative of already existing moderate instability in the atmosphere which built up further and eventually led to strong updraft during evening hours.

The vertical structure of the storm in terms of DWR polarimetric measurements and associated hydrometeor identification is shown in Figure 13. Averaged reflectivity between 2.5 and 3.5 km height during rapid initial development stage of the storm shows active convective regions (Figure 13a). Then a vertical cross section along the convection line AB has been considered to analyse the vertical structure of the storm. Figure 13b shows the vertical cross section of reflectivity at horizontal polarization (Z_h) along the convection line AB. The x-axis represents the distance from point A towards point B. Reflectivity values greater than 30 dBZ reaching up to 10 km height signifies the

existence of strong updraft within the convective core region. This strong updraft can keep the larger hydrometeors (bigger raindrops, graupels etc.) float aloft for longer period giving them more time to grow further by the collision-coalescence process for raindrops and by riming process for ice particles (Schuur et al. 2001). Since, reflectivity is proportional to the 6^{th} power of the particle diameter (Bringi & Chandrasekar 2001), these larger particles produce such strong reflectivity values even at higher altitudes.

Figure 13c shows the vertical cross section of differential reflectivity (Z_{dr}) along the convection line. Z_{dr} value gives a measure of the oblateness of precipitation particles and hence could be useful in distinguishing between larger raindrops, hail, and graupel due to differences in shape and orientation. Since raindrops (diameter> 1 mm) are deformed into oblate spheroid shape due to aerodynamic forces (Pruppacher & Beard, 1970) with a preferred orientation of their major axes in the horizontal direction (and therefore $Z_h > Z_v$), Z_{dr} is positive and increases with raindrop size. This increase in the value of Z_{dr} with raindrop size is shown quantitatively in Bringi et al. (2009) in terms of a polynomial fit between observed Z_{dr} and mean drop diameter measured by disdrometer. Z_{dr} values greater than 2 dB were observed which indicate presence of bigger raindrops or melting bigger ice particles (Anderson et al. 2011) below 4 km height. Bigger raindrops are also observed in the disdrometer measurements of rain DSD (Figure 9a).

Z_{dr} values are much smaller at higher altitudes (above 0° isotherm ~5 km height) as the ice particles such as aggregate, graupel, hail, tend to be spherically symmetric or tumble while falling, causing low values of Z_{dr}. The lower value of dielectric constant for ice compared to water is another factor behind lower Z_{dr} for ice particles. Within the strong convective region at heights above the melting layer, a higher value of Z_{dr} along with high value of K_{dp} indicates supercooled liquid drops above freezing level (Hubbert et al., 1998). The ρ_{hv} shows high values (>0.95) throughout the entire cross section (Figure 13d) and ρ_{hv} depends on several factors such as eccentricity, distribution of canting angle, irregular shape and mixture of different types of hydrometeors. Relatively lower values of ρ_{hv} at the central region and at higher altitudes within the cross-section, could be attributed to mixture of ice particles with rain.

The estimated K_{dp} (Figure 13e) shows that the spatial pattern of K_{dp} is in tandem with that of reflectivity though there are differences. High values (greater than 5° km^{-1}) of K_{dp} below melting level suggest the presence of intense convective precipitation with bigger raindrops formed due to

the coalescence process or due to melting graupel. As drop eccentricity increases with diameter, the differential propagation phase increases causing higher values of K_{dp} within regions of intense convective precipitation. A similar structure of K_{dp} within convective regions is reported by Ryzhkov et al. (2002). Higher values of K_{dp} above freezing level suggests prevalence of supercooled droplets which can help in formation of graupel particles via the riming process.

Identified hydrometeor types are shown in Figure 13f. Below the melting level, it is mainly dominated by rain (RN) and above melting level, ice aggregates (AG) are the dominating hydrometeors. At heights between 4.5 to 8 km, within the convective core regions graupel (HDG) particles are abundant. Similar findings are obtained in Dolan et al. (2013), in which HDG was found close to the melting level and LDG at higher heights. Within such convective cores reaching up to 10 km height, liquid droplets are pushed to heights much above the freezing level and they stay there as unstable supercooled droplets. Upon contact with ice-aggregates they immediately freeze onto the surface forming bigger ice particles viz. graupel. The strong updraft can sustain these graupels in air for longer helping them grow even further. The presence of vertical ice indicates the existence of electric field which forces these particles to orient vertically and this could be due to the charging via the collisions between graupels and smaller ice particles, as confirmed by different laboratory experiments (Takahashi, 1978; Jayaratne et al., 1983; Saunders et al., 1991).

3.2.3 Convective event on 25th May, 2018

An organized mesoscale convective system over southern peninsular India prior to the onset of the southwest monsoon occurred on 25th May, 2018 during 13:00-19:00 IST. The CAPE value of 148 J kg^{-1} was observed from the nearest radiosonde measurements in the morning hour (05:30 IST) and increased to 1092 J kg^{-1} in the afternoon hours (17:30 IST) suggesting the unstable layers favouring the formation of convective event. The development of the convective system is presented in the PPI diagrams of radar reflectivity field from 12:58 IST to 16:10 IST consecutive times during the event (Figure 14). Unlike the convective system on 13th May, this system started forming over the oceanic region (westward from radar) as well as over the land (north-east ward from radar) around 13:00 IST and gradually covered more and more region. Compared to the previous system, this system had a much larger spatial extent with a lower value of the peak reflectivity during the development stage, suggesting lesser convective activity compared to the 13th May event. Rainfall and the embedded rain DSD during the event were recorded by the disdrometer at NCESS (Figure 9b). The peak rain

rate (~10 mm h^{-1}) was significantly lower compared to that for the previous system (100 mm h^{-1}). The drops of diameter greater than 3 mm are absent on 25th May, 2018 suggesting lesser updraft speed and hence lesser time for the growth of raindrops. The spatial-temporal evolution of the brightness temperature (INSAT-3DR data) during the event (Figure 10f-10j & 11) reveals a slow development of the cloud system. The development is markedly different from the one on 13th May event, which was much more rapid. Around 15:30 IST the lowest brightness temperature of ~220 K was noted, which was significantly higher than the convective event on 13th May 2018 (<185 K), indicating less deep cloud systems. The ceilometer observation shows the presence of clouds having the base height below 5 km level (Figure 12b) during the initiation of the convective system. The dissipation phase of the event was registered with high level clouds (5 < CBH < 10 km) over the region.

The vertical structure inside the system is shown through a vertical cross along a convective region (Figure 15). The spatial distribution of the reflectivity averaged between 2.5 and 3.5 km height during developing stage is shown in Figure 15a. A vertical cross section along the line AB through the convective region is taken and hydrometeor identification has also been done. The overall features of the different variables are very much similar to those in Figure 13. The reflectivity core at a distance between 5 and 20 km from point A was observed and it reached up to a height of 7 km (Figure 15b), which was 10 km on 13th May event. The Z_{dr} values (Figure 15c) along the convection line are much lower due to smaller drop size as observed in the DSD from disdrometer. Values of ρ_{hv} (Figure 15d) are high (>0.9) indicating presence of rain with smaller drops at lower levels. The structure of K_{dp} (Figure 15e) follows the structure of Z_h but values are less (<4° km^{-1}) compared to that in 13th May case. This is mainly because of lower rain rate and relatively smaller drops with less eccentricity, resulting in smaller difference between the reflectivity at horizontal and vertical polarization. Identified hydrometeor types shown in Figure 15f are quite similar to the ones in 13th May case (Figure 13f). Rain (RN), aggregates (AG) and graupels (HDG) are the main hydrometeor types identified. The graupels are present mainly in the highest reflectivity column. In this case the abundance of graupels is much less compared to the 13th May case. This is because of lower updraft as inferred from the brightness temperature data. The occurrence of drizzle (DZ) types was also identified along the vertical cross section.

4. Summary

The present study is focused on the structure of pre-monsoon convective systems over a tropical coastal region in southern peninsular India. Observations from several instruments such as Doppler weather radar (DWR), disdrometer, ceilometer, INSAT-3DR satellite data, radiosonde measurements are used in the study. Using the quality controlled DWR data, 11 convective events have been identified by inspecting the reflectivity field from DWR. Out of which, the convective events occurred on 13th May and 25th May 2018 has been analysed in detail to understand the development of mesoscale cloud systems. Convective-stratiform separation has been done for all the events. Following are the major conclusions of the study.

- Convective-stratiform separation clearly demarcates the distinct difference in reflectivity profiles over convective and stratiform regions. A peak in the mean reflectivity profile near 3 km height is registered for convective regions. Stratiform regions are characterized by a peak reflectivity near melting layer signifying the bright band and almost constant reflectivity profile between 1km and 4 km levels. The distribution of the reflectivity values at a height of 3 km shows bell shaped nature and there is an overlap between distributions for the convective and stratiform precipitations. It also shows that using a single threshold for reflectivity or rain rate may not be useful for convective-stratiform separation.
- The reflectivity PPI captured the spatial and temporal evolution of the convective cases on 13th and 25th May 2018 from the initiation to the dissipative stages of both the events. The development of the system on 13th May was much more rapid with cloud tops reaching much higher altitudes as clearly seen in the brightness temperature observed from satellite. Disdrometer measurements of rain rate and DSD during the two events show that the event on 13th May, was associated with high rain rate (>100 mm h^{-1}) having bigger raindrops (diameter > 3mm) during the first hour of the event. Even though the spatial extent of the system on 25th May, was larger, much lower rain rate (<10 mm h^{-1}) with relatively smaller (diameter < 3 mm) raindrops was observed.
- Vertical structures inside the storms during rapid development stage have been obtained by taking vertical cross sections of reflectivity through major convective regions. The reflectivity values show convective cores reaching 10 km height on 13th May and about 7 km height on 25th May. High values of Z_{dr} at lower levels were observed on 13th May, due to the oblate spheroid shape of the bigger raindrops. The structure of K_{dp} field is quite similar to

that of reflectivity in both the cases. High values of K_{dp} reveals the presence of intense rainfall on 13th May, as K_{dp} is mainly dominated by bigger raindrops.

- Fuzzy-logic based hydrometeor identification (HID) has been done along the vertical cross sections over prominent convective regions. HID analysis shows presence of graupel at middle levels within the convective core regions revealing presence of strong updrafts. Ice aggregates and rain are the dominant hydrometeors above and below melting level respectively. Presence of vertical ice signifies the presence of electric field inside the storm. Such electric field may be generated due to non-inductive charging via collision between graupel and smaller ice crystals.

It would be worth studying the observed lightning activity (if any) during these events as presence of vertical ice indicates toward development of electric field. If major lightning activity occurred during these events, then it would support the collision charging mechanism as graupels are identified within the convective core regions.

Acknowledgments

The authors sincerely thank the Director, National Centre for Earth Science Studies (NCESS) for encouragement and support. The authors are grateful to Dr. D. Padmalal, Head, Atmospheric Science Group, for the insightful comments. The authors acknowledge the support of Mr. Vincent Ferrer on the topography map of the study area. The authors would like to acknowledge the Meteorological and Oceanographic Satellite Data Archival Centre (MOSDAC) of the Space Application Centre (SAC), ISRO for supplying the DWR and INSAT-3DR data.

Data Availability Statement

The Doppler weather radar data used in this study is freely available through the https://www.mosdac.gov.in/ server. The in-situ data used in this study will be shared on the acceptance of the manuscript.

References:

Abhilash, S., Das, S., Kalsi, S. R., Das Gupta, M., Mohankumar, K., George, J. P., Banerjee, S. K., Thampi, S. B., & Pradhan, D. (2007). Assimilation of Doppler weather radar observations in a mesoscale model for the prediction of rainfall associated with mesoscale convective systems. *Journal of Earth System Science*, *116*(4), 275–304. https://doi.org/10.1007/s12040-007-0026-2

Agnihotri, G., Gouda, K. C., & Das, S. (2021). Characteristics of pre-monsoon convective systems over south peninsular India and neighborhood using tropical rainfall measuring mission's precipitation radar. *Meteorology and Atmospheric Physics*, *133*(2), 193–203. https://doi.org/10.1007/s00703-020-00740-7

Anderson, M. E., Carey, L. D., Petersen, W. A., & Knupp, K. R. (2011). C-band dual-polarimetric radar signatures of hail. *Electronic Journal of Operational Meteorology*, *12*(2), 1–30.

Aydin, K., Bringi, V. N., & Liu L. (2000). Rain-Rate Estimation in the Presence of Hail Using S-Band Specific Differential Phase and Other Radar Parameters. *Journal of Applied Meteorology*, *34*(2), 404–410. https://doi.org/10.1175/1520-0450-34.2.404

Balakrishnan, N., & Zrnić, D. S. (1990). Estimation of rain and hail rates in mixed-phase precipitation. *Journal of Atmospheric Sciences*, *47*(5), 565-583. https://doi.org/10.1175/1520-0469(1990)047%3C0565:EORAHR%3E2.0.CO;2

Bhardwaj, P., & Singh, O. (2018). Spatial and temporal analysis of thunderstorm and rainfall activity over India. *Atmosfera*, *31*(3), 255–284. https://doi.org/10.20937/ATM.2018.31.03.04

Biggerstaff, M. I., & Listemaa, S. A. (2000). An improved scheme for convective/stratiform echo classification using radar reflectivity. *Journal of Applied Meteorology*, *39*(12), 2129–2150. https://doi.org/10.1175/1520-0450(2001)040<2129:AISFCS>2.0.CO;2

Bringi, V. N., and Chandrasekar, V. (2001): Polarimetric Doppler Weather Radar: Principles and Applications. Cambridge University Press, 636 pp.

Bringi, V. N., Chandrasekar, V., Hubbert, J., Gorgucci, E., Randeu, W. L., & Schoenhuber, M. (2003). Raindrop size distribution in different climatic regimes from disdrometer and dual-polarized radar analysis. *Journal of the Atmospheric Sciences*, *60*(2), 354–365. https://doi.org/10.1175/1520-0469(2003)060<0354:RSDIDC>2.0.CO;2

Bringi, V. N., Thurai, M., Nakagawa, K., Huang, G. J., Kobayashi, T., Adachi, A., Hanado, H., & Sekizawa, S. (2006). Rainfall estimation from C-band polarimetric radar in Okinawa, Japan:

614 Comparisons with 2D-video disdrometer and 400 MHz wind profiler. *Journal of the*
615 *Meteorological Society of Japan*, *84*(4), 705–724. https://doi.org/10.2151/jmsj.84.705

616 Bringi, V. N., Williams, C. R., Thurai, M., & May, P. T. (2009). Using dual-polarized radar and
617 dual-frequency profiler for DSD characterization: A case study from Darwin, Australia. *Journal*
618 *of Atmospheric and Oceanic Technology*, *26*(10), 2107–2122.
619 https://doi.org/10.1175/2009JTECHA1258.1

620 Cecil, D. J., Buechler, D. E., & Blakeslee, R. J. (2014). Gridded lightning climatology from TRMM-
621 LIS and OTD: Dataset description. *Atmospheric Research*, *135–136*, 404–414.
622 https://doi.org/10.1016/j.atmosres.2012.06.028

623 Chandrasekar, V., Bringi, V. N., Balakrishnan, N., & Zrnić, D. S. (1990). Error structure of
624 multiparameter radar and surface measurements of rainfall. Part III: Specific differential
625 phase. *Journal of Atmospheric and Oceanic Technology*, *7*(5), 621-629.
626 https://doi.org/10.1175/1520-0426(1990)007%3C0621:ESOMRA%3E2.0.CO;2

627 Christian, H. J., Blakeslee, R. J., Boccippio, D. J., Boeck, W. L., Buechler, D. E., Driscoll, K. T.,
628 Goodman, S. J., Hall, J. M., Koshak, W. J., Mach, D. M., & Stewart, M. F. (2003). Global
629 frequency and distribution of lightning as observed from space by the Optical Transient
630 Detector. *Journal of Geophysical Research: Atmospheres*, *108*(1).
631 https://doi.org/10.1029/2002jd002347

632 Cifelli, R., Chandrasekar, V., Lim, S., Kennedy, P. C., Wang, Y., & Rutledge, S. A. (2011). A new
633 dual-polarization radar rainfall algorithm: Application in Colorado precipitation events.
634 *Journal of Atmospheric and Oceanic Technology*, *28*(3), 352–364.
635 https://doi.org/10.1175/2010JTECHA1488.1

636 Clothiaux, E. E., Ackerman, T. P., Mace, G. G., Moran, K. P., Marchand, R. T., Miller, M. A., &
637 Martner, B. E. (2000). Objective determination of cloud heights and radar reflectivities using a
638 combination of active remote sensors at the ARM CART sites. *Journal of Applied*
639 *Meteorology*, *39*(5), 645-665. https://doi.org/10.1175/1520-
640 0450(2000)039%3C0645:ODOCHA%3E2.0.CO;2

641 Dhawan, V. B., Tyagi, A., & Bansal, M. C. (2008). Forecasting of thunderstorms in pre-monsoon
642 season over northwest India. *Mausam*, *59*(4), 433–444.

643 Dolan, B., & Rutledge, S. A. (2009). A theory-based hydrometeor identification algorithm for X-
644 band polarimetric radars. *Journal of Atmospheric and Oceanic Technology*, *26*(10), 2071–2088.
645 https://doi.org/10.1175/2009JTECHA1208.1

646 Dolan, B., Rutledge, S. A., Lim, S., Chandrasekar, V., & Thurai, M. (2013). A robust C-band
647 hydrometeor identification algorithm and application to a long-term polarimetric radar dataset.
648 *Journal of Applied Meteorology and Climatology*, *52*(9), 2162–2186.
649 https://doi.org/10.1175/JAMC-D-12-0275.1

650 Doviak, R.J. and Zrni´c, D.S. *Doppler Radar and Weather Observations*. 2nd edition, San Diego,
651 CA, Academic Press, 1993.

652 Elio, R., Haan, J. D., & Strong, G. S. (1987). METEOR: An artificial intelligence system for
653 convective storm forecasting. *Journal of Atmospheric and Oceanic Technology*, *4*(1), 19-28.
654 https://doi.org/10.1175/1520-0426(1987)004%3C0019:MAAISF%3E2.0.CO;2

655 Farr, T. G., Rosen, P. A., Caro, E., Crippen, R., Duren, R., Hensley, S., ... & Alsdorf, D. (2007). The
656 shuttle radar topography mission. *Reviews of geophysics*, *45*(2).
657 https://doi.org/10.1029/2005RG000183

658 Friedrich, K., Hagen, M., & Einfalt, T. (2006). A quality control concept for radar reflectivity,
659 polarimetric parameters, and Doppler velocity. *Journal of Atmospheric and Oceanic*
660 *Technology*, *23*(7), 865–887. https://doi.org/10.1175/JTECH1920.1

661 Friedrich, K., Higgins, S., Masters, F. J., & Lopez, C. R. (2013). Articulating and stationary
662 PARSIVEL disdrometer measurements in conditions with strong winds and heavy
663 rainfall. *Journal of Atmospheric and Oceanic Technology*, *30*(9), 2063-2080.
664 https://doi.org/10.1175/JTECH-D-12-00254.1

665 Halder, M., & Mukhopadhyay, P. (2016). Microphysical processes and hydrometeor distributions
666 associated with thunderstorms over India: WRF (cloud-resolving) simulations and validations
667 using TRMM. *Natural Hazards*, *83*(2), 1125–1155. https://doi.org/10.1007/s11069-016-2365-
668 2

669 Heese, B., Flentje, H., Althausen, D., Ansmann, A., & Frey, S. (2010). Ceilometer lidar comparison:
670 backscatter coefficient retrieval and signal-to-noise ratio determination. *Atmospheric*
671 *Measurement Techniques*, *3*(6), 1763-1770. https://doi.org/10.5194/amt-3-1763-2010

672 Houze, R. A. (1997). Stratiform Precipitation in Regions of Convection: A Meteorological Paradox?
673 *Bulletin of the American Meteorological Society*, *78*(10), 2179–2196.
674 https://doi.org/10.1175/1520-0477(1997)078<2179:SPIROC>2.0.CO;2

675 Hubbert, J., Bringi, V. N., Carey, L. D., & Bolen, S. (1998). CSU-CHILL polarimetric radar
676 measurements from a severe hail storm in eastern Colorado. *Journal of Applied Meteorology*,
677 *37*(8), 749–775. https://doi.org/10.1175/1520-0450(1998)037<0749:CCPRMF>2.0.CO;2

678 Hubbert, J., Chandrasekar, V., Bringi, V. N., & Meischner, P. (1993). Processing and interpretation
679 of coherent dual-polarized radar measurements. *Journal of Atmospheric and Oceanic*
680 *Technology*, *10*(2), 155-164. https://doi.org/10.1175/1520-
681 0426(1993)010%3C0155:PAIOCD%3E2.0.CO;2

682 Islam, T., Rico-Ramirez, M. A., Han, D., & Srivastava, P. K. (2012). Artificial intelligence
683 techniques for clutter identification with polarimetric radar signatures. *Atmospheric Research*,
684 *109–110*, 95–113. https://doi.org/10.1016/j.atmosres.2012.02.007

Jameson, A. (1985). Microphysical interpretation of multiparameter radar measurements in rain. Part III: Interpretation and measurement of propagation differential phase shift between orthogonal linear polarizations. *Journal of Atmospheric Sciences*, *42*(6), 607-614. https://doi.org/10.1175/1520-0469(1985)042%3C0607:MIOMRM%3E2.0.CO;2

Jash, D., Resmi, E. A., Unnikrishnan, C. K., Sumesh, R. K., Sreekanth, T. S., Sukumar, N., & Ramachandran, K. K. (2019). Variation in rain drop size distribution and rain integral parameters during southwest monsoon over a tropical station: An inter-comparison of disdrometer and Micro Rain Radar. *Atmospheric Research*, *217*, 24–36. https://doi.org/10.1016/j.atmosres.2018.10.014

Jayaratne, E. R., Saunders, C. P. R., & Hallett, J. (1983). Laboratory studies of the charging of soft-hail during ice crystal interactions. *Quarterly Journal of the Royal Meteorological Society*, *109*(461), 609-630. https://doi.org/10.1256/smsqj.46110

Keenan, T. (2003). Hydrometeor classification with a C-band polarimetric radar. *Australian Meteorological Magazine*, *52*(1), 23–31.

Kumar, K. K., Subrahmanyam, K. V., Kumar, C. P., Shanmugasundari, J., Koushik, N., Ajith, R. P., & Devi, L. G. (2020). C-band dual-polarization Doppler weather radar at Thumba (8.537 N, 76.865 E): initial results and validation. *Journal of Applied Remote Sensing*, *14*(4), 044509. https://doi.org/10.1117/1.JRS.14.044509

Lakshmanan, V., Karstens, C., Krause, J., & Tang, L. (2014). Quality control of weather radar data using polarimetric variables. *Journal of Atmospheric and Oceanic Technology*, *31*(6), 1234–1249. https://doi.org/10.1175/JTECH-D-13-00073.1

Leena, P. P., Pandithurai, G., Gayatri, K., Murugavel, P., Ruchith, R. D., Sakharam, S., Dani, K. K., Patil, C., Dharmaraj, T., Patil, M. N., & Prabhakaran, T. (2019). Analysing the characteristic features of a pre-monsoon thunderstorm event over Pune, India, using ground-based observations and WRF model. *Journal of Earth System Science*, *128*(4). https://doi.org/10.1007/s12040-019-1136-3

Litta, A. J., & Mohanty, U. C. (2008). Simulation of a severe thunderstorm event during the field experiment of STORM programme 2006, using WRF-NMM model. *Current Science*, *95*(2), 204–215.

Litta, A. J., Mohanty, U. C., Das, S., & Mary Idicula, S. (2012). Numerical simulation of severe local storms over east India using WRF-NMM mesoscale model. *Atmospheric Research*, *116*, 161–184. https://doi.org/10.1016/j.atmosres.2012.04.015

Liu, H., & Chandrasekar, V. (2000). Classification of hydrometeors based on polarimetric radar measurements: Development of fuzzy logic and neuro-fuzzy systems, and in situ verification. *Journal of Atmospheric and Oceanic Technology*, *17*(2), 140–164. https://doi.org/10.1175/1520-0426(2000)017<0140:COHBOP>2.0.CO;2

Löffler-Mang, M., & Joss, J. (2000). An optical disdrometer for measuring size and velocity of hydrometeors. *Journal of Atmospheric and Oceanic Technology*, *17*(2), 130-139. https://doi.org/10.1175/1520-0426(2000)017<0130:AODFMS>2.0.CO;2

Madhulatha, A., & Rajeevan, M. (2018). Impact of different parameterization schemes on simulation of mesoscale convective system over south-east India. *Meteorology and Atmospheric Physics*, *130*(1), 49–65. https://doi.org/10.1007/s00703-017-0502-4

Manohar, G. K., & Kesarkar, A. P. (2004). Climatology of thunderstorm activity over the Indian region : II . Spatial distribution. *Mausam*, *1*(January), 31–40.

Marzano, F. S., Scaranari, D., Celano, M., Alberoni, P. P., Vulpiani, G., & Montopoli, M. (2006). Hydrometeor classification from dual-polarized weather radar: Extending fuzzy logic from S-band to C-band data. *Advances in Geosciences*, *7*, 109–114. https://doi.org/10.5194/adgeo-7-109-2006

Mishra, S., Shanmuga Sundari, J., Channabasava, B., & Anandan, V. K. (2020). First indigenously developed polarimetric C-band Doppler weather radar in India and its first hand validation results. *Journal of Electromagnetic Waves and Applications*, *34*(6), 825–840. https://doi.org/10.1080/09205071.2020.1742798

Mukhopadhyay, P., Mahakur, M., & Singh, H. A. K. (2009). The interaction of large scale and mesoscale environment leading to formation of intense thunderstorms over Kolkata part I: Doppler radar and satellite observations. *Journal of Earth System Science*, *118*(5), 441–466. https://doi.org/10.1007/s12040-009-0046-1

Parks, T. W. & Burrus C. S., *Digital Filter Design*, John Wiley & Sons, 1987, chapter 7

Proakis, J. G., & Manolakis, D. G. (1988). *Introduction to digital signal processing*. MacMillan Publishing Company.

Pruppacher, H. R., & Beard, K. V. (1970). A wind tunnel investigation of the internal circulation and shape of water drops falling at terminal velocity in air. *Quarterly Journal of the Royal Meteorological Society*, *96*(408), 247–256. https://doi.org/10.1002/qj.49709640807

Purdom, J. F. W. (2003). *Local severe storm monitoring and prediction using satellite data*. *1*(January), 141–154.

Rajeevan, M., Kesarkar, A., Thampi, S. B., Rao, T. N., Radhakrishna, B., & Rajasekhar, M. (2010). Sensitivity of WRF cloud microphysics to simulations of a severe thunderstorm event over Southeast India. *Annales Geophysicae*, *28*(2), 603–619. https://doi.org/10.5194/angeo-28-603-2010

Rajeevan, M., Madhulatha, A., Rajasekhar, M., Bhate, J., Kesarkar, A., & Appa Rao, B. V. (2012). Development of a perfect prognosis probabilistic model for prediction of lightning over south-

east India. *Journal of Earth System Science*, *121*(2), 355–371. https://doi.org/10.1007/s12040-012-0173-y

Rao, Y. P., & Srinivasan, V. (1969). Discussion of typical synoptic weather situation: winter western disturbances and their associated features. *Indian Meteorological Department: Forecasting Manual Part III*.

Ravi, N., Mohanty, U. C., Madan, O. P., & Paliwal, R. K. (1999). Forecasting of thunderstorms in the pre-monsoon season at Delhi. *Meteorological Applications*, *6*(1), 29–38. https://doi.org/10.1017/S1350482799000973

Romatschke, U., & Houze, R. A. (2011). Characteristics of precipitating convective systems in the premonsoon season of South Asia. *Journal of Hydrometeorology*, *12*(2), 157–180. https://doi.org/10.1175/2010JHM1311.1

Roy, S. Sen, Mohapatra, M., Tyagi, A., & Roy Bhowmik, S. K. (2019). A review of nowcasting of convective weather over the Indian region. *Mausam*, *70*(3), 465–484. https://doi.org/10.54302/mausam.v70i3.227

Ryzhkov, A. V., & Zrnic, D. S. (1998). Polarimetric rainfall estimation in the presence of anomalous propagation. *Journal of Atmospheric and Oceanic Technology*, *15*(6), 1320–1330. https://doi.org/10.1175/1520-0426(1998)015<1320:PREITP>2.0.CO;2

Ryzhkov, A. V., Zrnic, D. S., Hubbert, J. C., Bringi, V. N., Vivekanandan, J., & Brandes, E. A. (2002). Polarimetric radar observations and interpretation of co-cross-polar correlation coefficients. *Journal of Atmospheric and Oceanic Technology*, *19*(3), 340–354. https://doi.org/10.1175/1520-0426-19.3.340

Sad, H. P., Kumar, P., & Panda, S. K. (2021). Doppler weather radar data assimilation at convective-allowing grid spacing for predicting an extreme weather event in Southern India. *International Journal of Remote Sensing*, *42*(10), 3681–3707. https://doi.org/10.1080/01431161.2021.1880660

Saha, U., Maitra, A., Midya, S. K., & Das, G. K. (2014). Association of thunderstorm frequency with rainfall occurrences over an Indian urban metropolis. *Atmospheric Research*, *138*, 240–252. https://doi.org/10.1016/j.atmosres.2013.11.021

Saunders, C. P. R., Keith, W. D., & Mitzeva, R. P. (1991). The effect of liquid water on thunderstorm charging. *Journal of Geophysical Research: Atmospheres*, *96*(D6), 11007-11017. https://doi.org/10.1029/91JD00970

Schuur, T. J., Ryzhkov, A. V., Zrnic, D. S., & Schönhuber, M. (2001). Drop size distributions measured by a 2D video disdrometer: Comparison with dual-polarization radar data. *Journal of Applied Meteorology*, *40*(6), 1019–1034. https://doi.org/10.1175/1520-0450(2001)040<1019:DSDMBA>2.0.CO;2

Seliga, T. A., & Bringi, V. N. (1978). Differential reflectivity and differential phase shift: Applications in radar meteorology. *Radio Science*, *13*(2), 271-275. https://doi.org/10.1029/RS013i002p00271

Singh, O., & Bhardwaj, P. (2019). Spatial and temporal variations in the frequency of thunderstorm days over India. *Weather*, *74*(4), 138–144. https://doi.org/10.1002/wea.3080

Sisodiya, A., Pattnaik, S., & Baisya, H. (2020). Characterization of Different Rainfall Types from Surface Observations Over a Tropical Location. *Pure and Applied Geophysics*, *177*(2), 1111–1123. https://doi.org/10.1007/s00024-019-02338-6

Srivastava, K., Roy Bhowmik, S. K., Sen Roy, S., Thampi, S. B., & Reddy, Y. K. (2010). Simulation of high impact convective events over Indian region by ARPS model with assimilation of doppler weather radar radial velocity and reflectivity. *Atmosfera*, *23*(1), 53–73.

Steiner, M., Houze Jr, R. A., & Yuter, S. E. (1995). Climatological characterization of three-dimensional storm structure from operational radar and rain gauge data. *Journal of Applied Meteorology and Climatology*, *34*(9), 1978-2007. https://doi.org/10.1175/1520-0450(1995)034%3C1978:CCOTDS%3E2.0.CO;2

Subrahmanyam, K. V., & Baby, S. R. (2020). C-band Doppler weather radar observations during the passage of tropical cyclone 'Ockhi.' *Natural Hazards*, *104*(3), 2197–2211. https://doi.org/10.1007/s11069-020-04268-2

Sumesh, R. K., Resmi, E. A., Unnikrishnan, C. K., Jash, D., & Ramachandran, K. K. (2021). Signatures of shallow and deep clouds inferred from precipitation microphysics over windward side of Western Ghats. *Journal of Geophysical Research: Atmospheres*, *126*(10), e2020JD034312. https://doi.org/10.1029/2020JD034312

Suresh, R. (2012). Forecasting and nowcasting convective weather phenomena over southern peninsular india - part I: Thunderstorms. *Indian Journal of Radio and Space Physics*, *41*(4), 421–434.

Takahashi, T. (1978). Riming electrification as a charge generation mechanism in thunderstorms. *Journal of Atmospheric Sciences*, *35*(8), 1536-1548. https://doi.org/10.1175/1520-0469(1978)035%3C1536:REAACG%3E2.0.CO;2

Testud, J., Oury, S., Black, R. A., Amayenc, P., & Dou, X. (2001). The concept of "normalized" distribution to describe raindrop spectra: A tool for cloud physics and cloud remote sensing. *Journal of Applied Meteorology*, *40*(6), 1118–1140. https://doi.org/10.1175/1520-0450(2001)040<1118:TCONDT>2.0.CO;2

Thakur, S., Mondal, I., Ghosh, P. B., & De, T. K. (2019). Thunderstorm characteristics over the northeastern region (NER) of India during the pre-monsoon season, 2011 using geosynchronous satellite data. In *Advances in Intelligent Systems and Computing* (Vol. 813). Springer Singapore. https://doi.org/10.1007/978-981-13-1498-8_26

826 Thurai, M., Bringi, V. N., & May, P. T. (2010). CPOL radar-derived drop size distribution statistics
827 of stratiform and convective rain for two regimes in Darwin, Australia. *Journal of Atmospheric*
828 *and Oceanic Technology*, *27*(5), 932–942. https://doi.org/10.1175/2010JTECHA1349.1

829 Tokay, A., & Short, D. A. (1996). Evidence from tropical raindrop spectra of the origin of rain from
830 stratiform versus convective clouds. *Journal of Applied Meteorology and Climatology*, *35*(3),
831 355-371. https://doi.org/10.1175/1520-0450(1996)035%3C0355:EFTRSO%3E2.0.CO;2

832 Tyagi, A., Sikka, D. R., Goyal, S., & Bhowmick, M. (2012). A satellite based study of pre-monsoon
833 thunderstorms (Nor'westers) over eastern India and their organization into mesoscale
834 convective complexes. *Mausam*, *63*(1), 29–54.

835 Ulbrich, C. W., & Atlas, D. (2002). On the separation of tropical convective and stratiform rains.
836 *Journal of Applied Meteorology*, *41*(2), 188–195. https://doi.org/10.1175/1520-
837 0450(2002)041<0188:OTSOTC>2.0.CO;2

838 Umakanth, N., Satyanarayana, G. C., Naveena, N., Srinivas, D., & Rao, D. V. B. (2021). Statistical
839 and dynamical based thunderstorm prediction over southeast India. *Journal of Earth System*
840 *Science*, *130*(2). https://doi.org/10.1007/s12040-021-01561-x

841 Unal, C. (2009). Spectral polarimetric radar clutter suppression to enhance atmospheric echoes.
842 *Journal of Atmospheric and Oceanic Technology*, *26*(9), 1781–1797.
843 https://doi.org/10.1175/2009JTECHA1170.1

844 Unnikrishnan, C. K., Pawar, S., & Gopalakrishnan, V. (2021). Satellite-observed lightning hotspots
845 in India and lightning variability over tropical South India. *Advances in Space Research*.

846 Vivekanandan, J., Zrnic, D. S., Ellis, S. M., Oye, R., Ryzhkov, A. V., & Straka, J. (1999). Cloud
847 Microphysics Retrieval Using S-Band Dual-Polarization Radar Measurements. *Bulletin of the*
848 *American Meteorological Society*, *80*(3), 381–388. https://doi.org/10.1175/1520-
849 0477(1999)080<0381:CMRUSB>2.0.CO;2

850 Wang, Y., & Chandrasekar, V. (2009). Algorithm for estimation of the specific differential phase.
851 *Journal of Atmospheric and Oceanic Technology*, *26*(12), 2565–2578.
852 https://doi.org/10.1175/2009JTECHA1358.1

853 Williams, C. R., Ecklund, W. L., & Gage, K. S. (1995). Classification of precipitating clouds in the
854 tropics using 915-MHz wind profilers. *Journal of Atmospheric and Oceanic Technology*, *12*(5),
855 996-1012. https://doi.org/10.1175/1520-0426(1995)012%3C0996:COPCIT%3E2.0.CO;2

856 You, C. H., Lee, D. I., & Kang, M. Y. (2014). Rainfall estimation using specific differential phase
857 for the first operational polarimetric radar in Korea. *Advances in Meteorology*, *2014*.
858 https://doi.org/10.1155/2014/413717

Zhou, K., Zheng, Y., Li, B., Dong, W., & Zhang, X. (2019). Forecasting Different Types of Convective Weather: A Deep Learning Approach. *Journal of Meteorological Research*, *33*(5), 797–809. https://doi.org/10.1007/s13351-019-8162-6

Zipser, E. J., & Lutz, K. R. (1994). The vertical profile of radar reflectivity of convective cells: A strong indicator of storm intensity and lightning probability?. *Monthly Weather Review*, *122*(8), 1751-1759. https://doi.org/10.1175/1520-0493(1994)122%3C1751:TVPORR%3E2.0.CO;2

Zrnić, D. S., & Ryzhkov, A. (1996). Advantages of rain measurements using specific differential phase. *Journal of Atmospheric and Oceanic Technology*, *13*(2), 454-464. https://doi.org/10.1175/1520-0426(1996)013%3C0454:AORMUS%3E2.0.CO;2

Zrnic, D. S., & Ryzhkov, A. V. (1999). Polarimetry for Weather Surveillance Radars. *Bulletin of the American Meteorological Society*, *80*(3), 389–406. https://doi.org/10.1175/1520-0477(1999)080<0389:PFWSR>2.0.CO;2

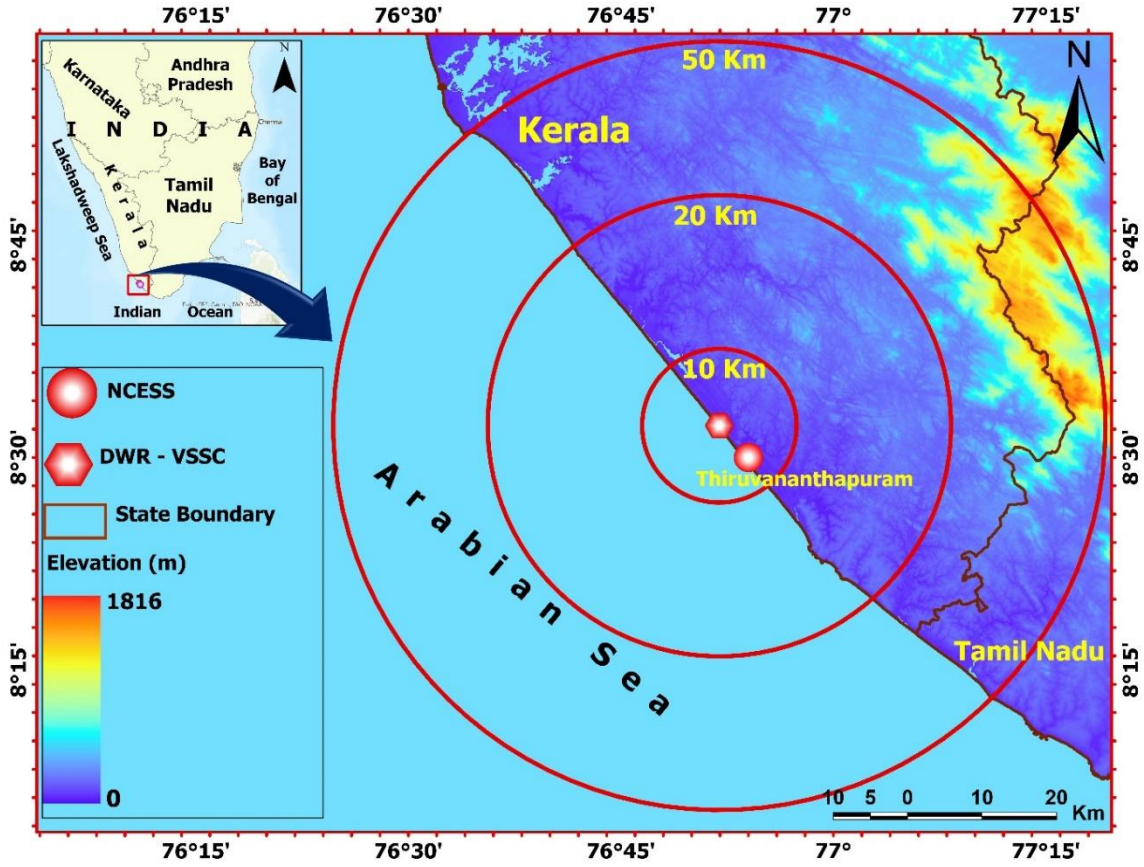

Figure 1. Terrain height (m) over the study area and the locations of the C- band DWR and NCESS observatory are given. Concentric circles represent distance from the radar for better reference.

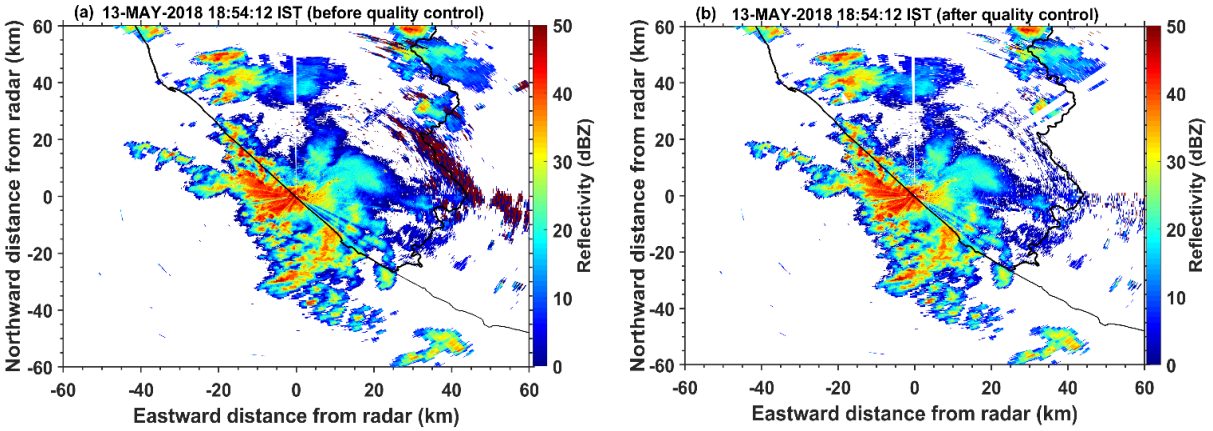

Figure 2. PPI diagrams of radar reflectivity at 2° elevation (a) before quality control and (b) after quality control at 18:54:12 IST, 13th May, 2018.

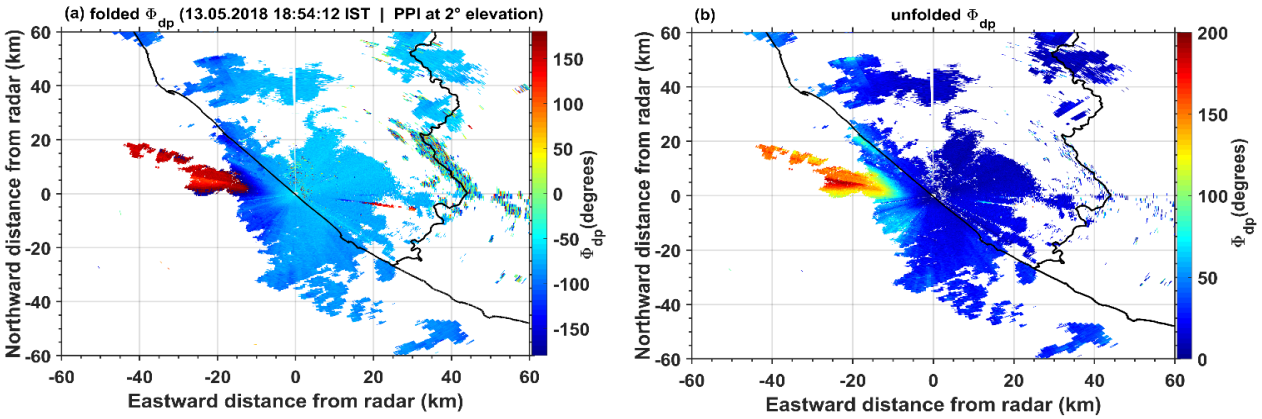

915

916 **Figure 3.** PPI diagrams at 2° elevation of (a) folded φ_{dp} and (b) unfolded φ_{dp} at 18:54:12 IST, 13th
917 May, 2018.
918

919

920

921

922

923

924

925

926

927

928

929

930

931

932

933

934

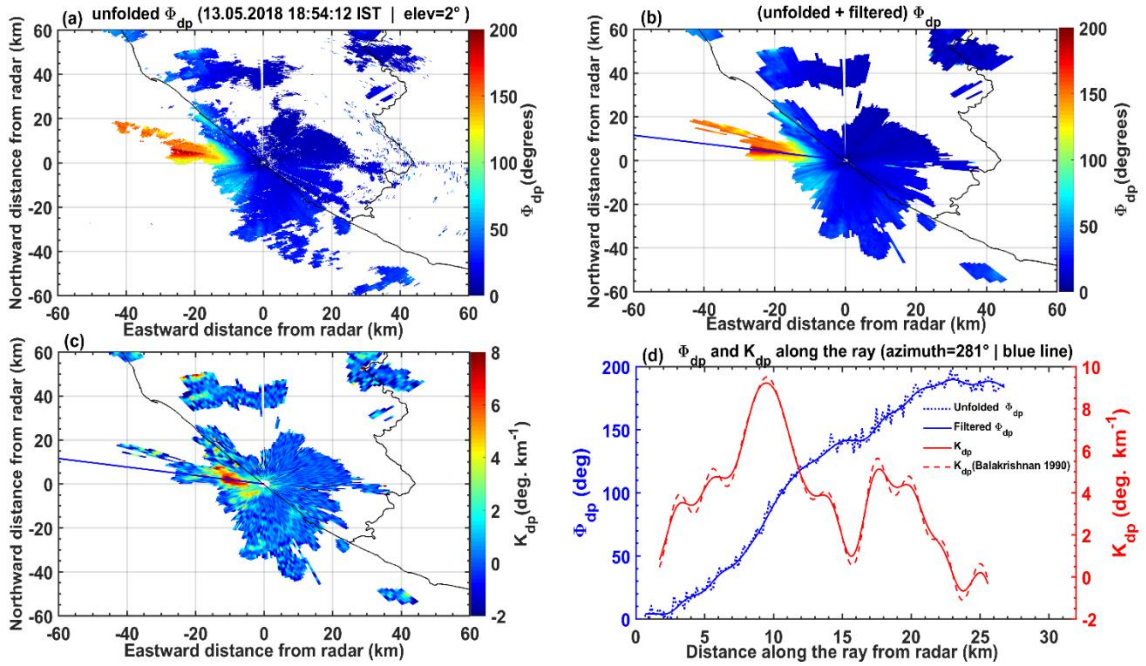

Figure 4. PPI at 2° elevation of (a)unfolded φ_{dp}, (b)filtered φ_{dp} and (c)estimated K_{dp}. Blue line in (b, c) represents 281° azimuth. (d) Variation of φ_{dp}(blue) and K_{dp}(red) along 281° azimuth. DATA: 18:54:12 IST, 13-may-2018.

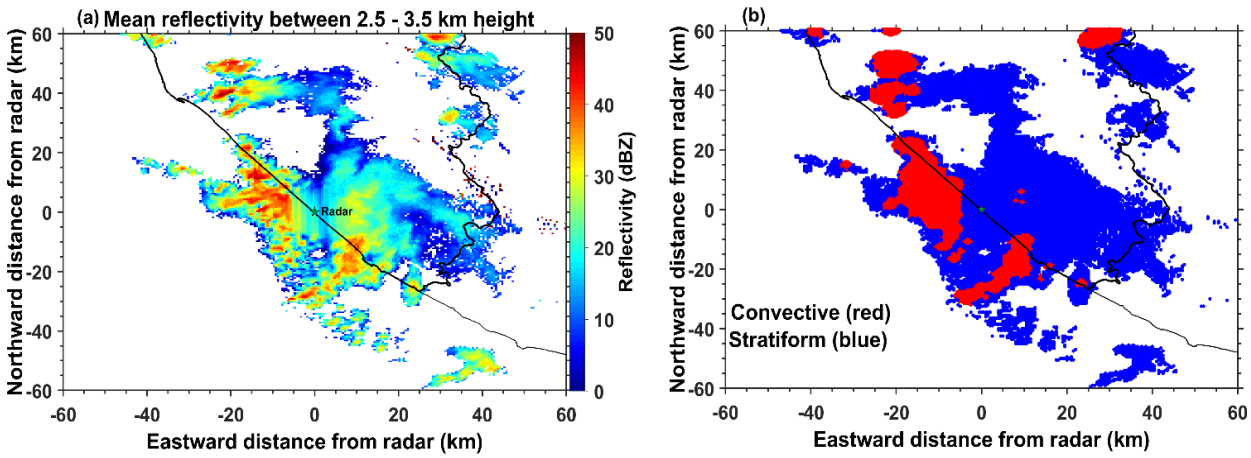

Figure 5. (a) PPI diagrams of radar reflectivity at 2° elevation averaged between 2.5 - 3.5 km height at 18:54:12 IST, on 13th May, 2018 and (b) the identified convective (red) and stratiform (blue) regions.

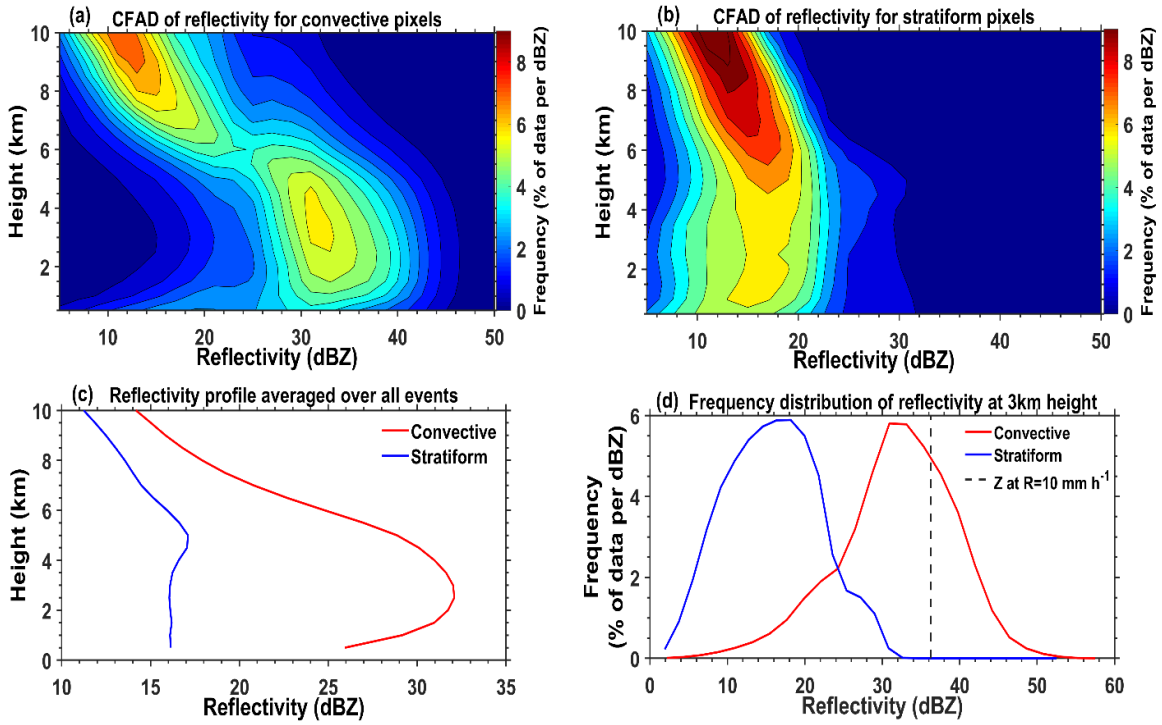

Figure 6. Contour frequency by altitude diagram (CFAD) of radar reflectivity for (a) convective and (b) stratiform regions. (c) Mean vertical profile of reflectivity over convective (red) and stratiform (blue) regions, (d) frequency distribution of reflectivity at 3 km height. The dotted line represents rain rate of 10 mm h^{-1}.

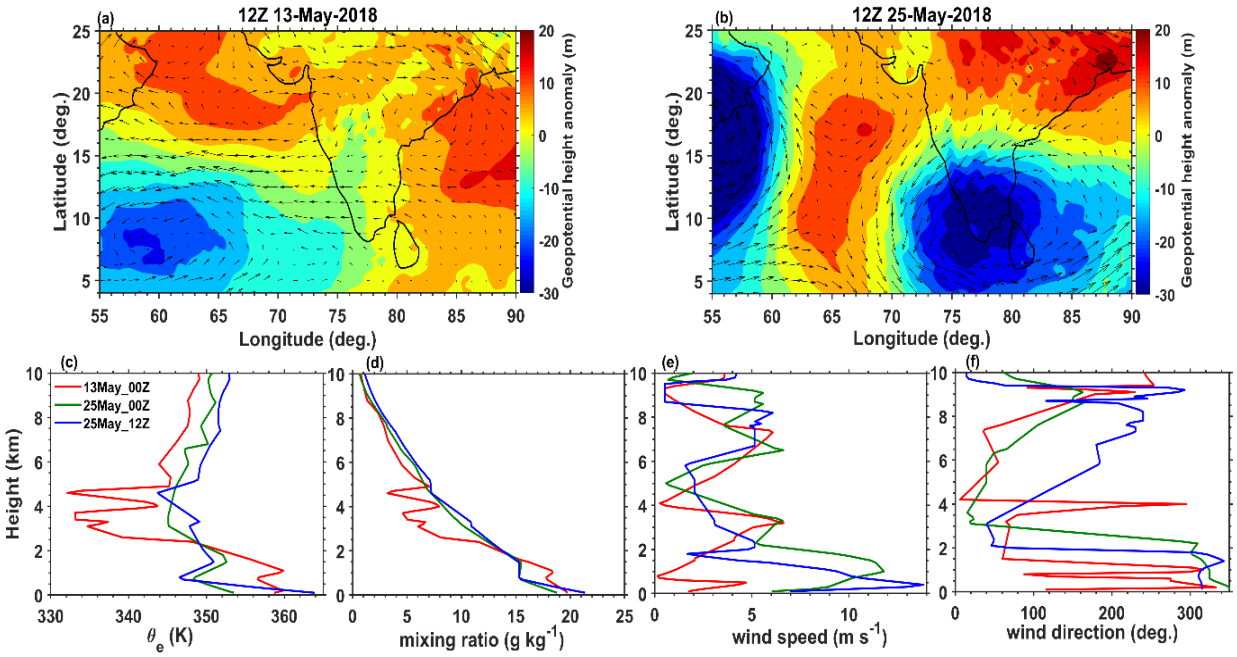

Figure 7. Horizontal wind vectors overlaid with geopotential height anomaly on (a) 13th May 2018 at 12Z, (b) 25th May 2018 at 12Z using ERA5 dataset. Vertical profiles of (c) θ_e, (d) mixing ratio, (e) wind speed and (f) wind direction on 13th May 2018 at 00Z (red), 25th May 2018 at 00Z (green) and 25th May 2018 at 12Z (blue) from radiosonde.

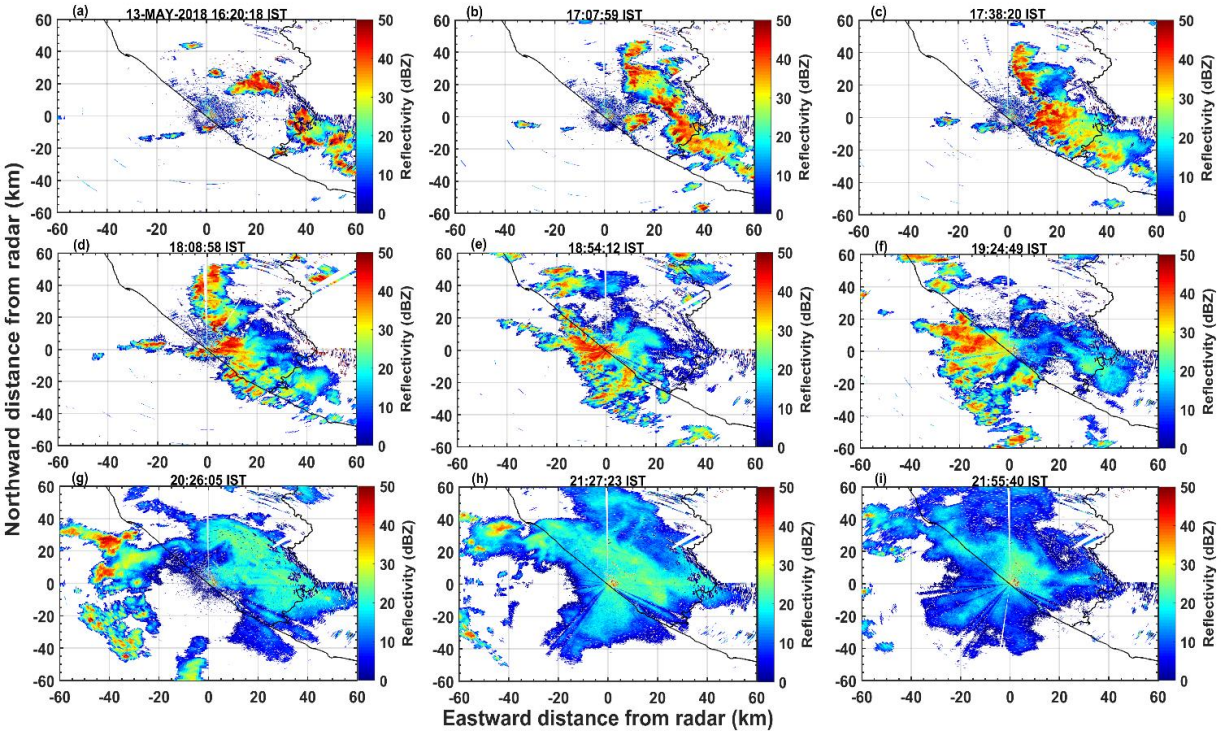

Figure 8. PPI diagrams of radar reflectivity at 2° elevation angle at 16:20:18 IST to 21:55:40 IST (a-i) during the event on 13th May, 2018.

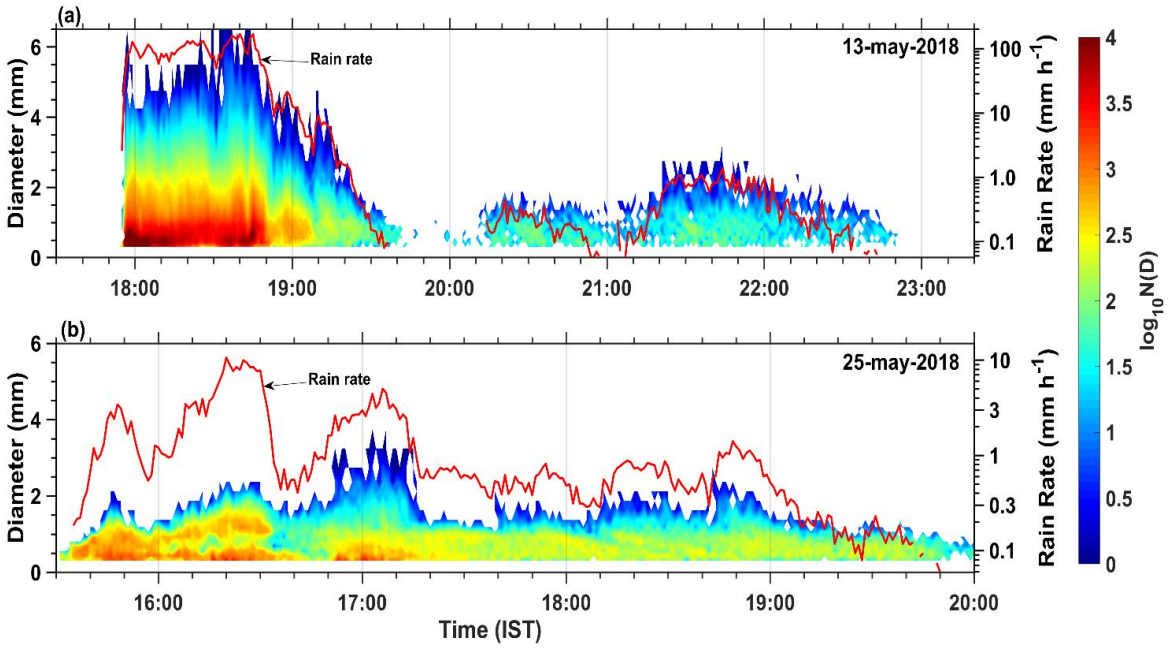

Figure 9. Time series of rain rate (red curve) overlaid with rain DSD (colour bar) during the convective events on (a) 13th May, 2018 and (b) 25th May, 2018 using disdrometer data.

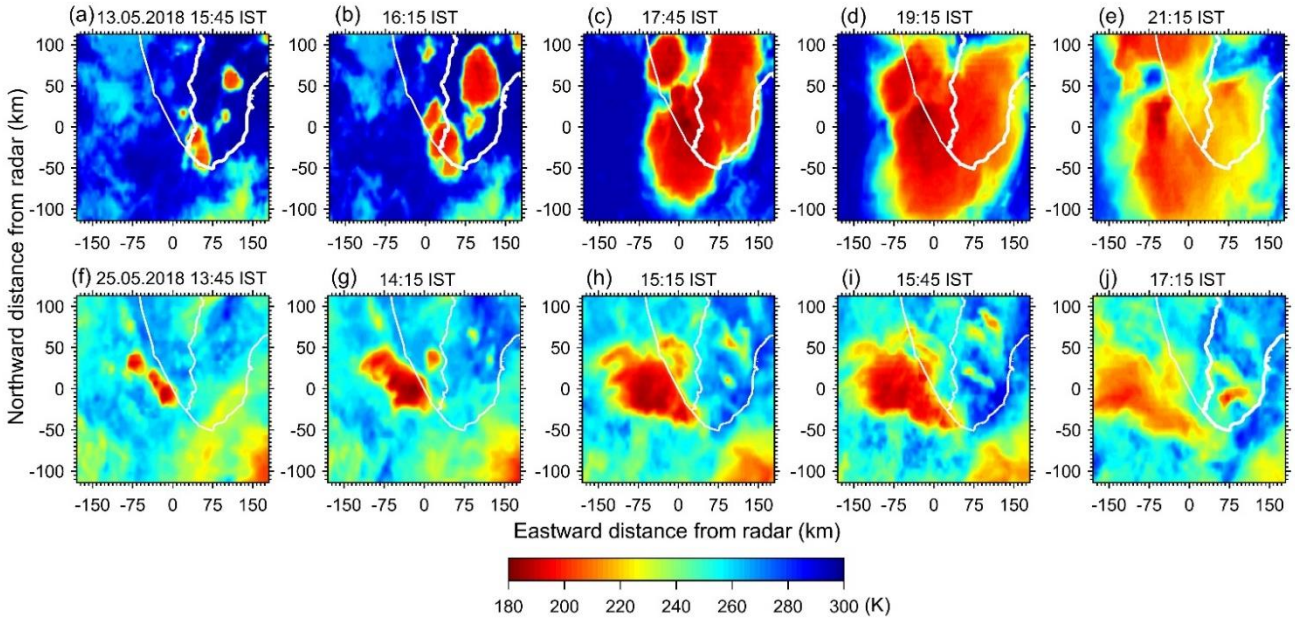

Figure 10. Spatial-temporal evolution of infrared brightness temperature during the convective events on 13th May, 2018 (a-e) and 25th May, 2018 (f-j) using INSAT-3DR satellite data.

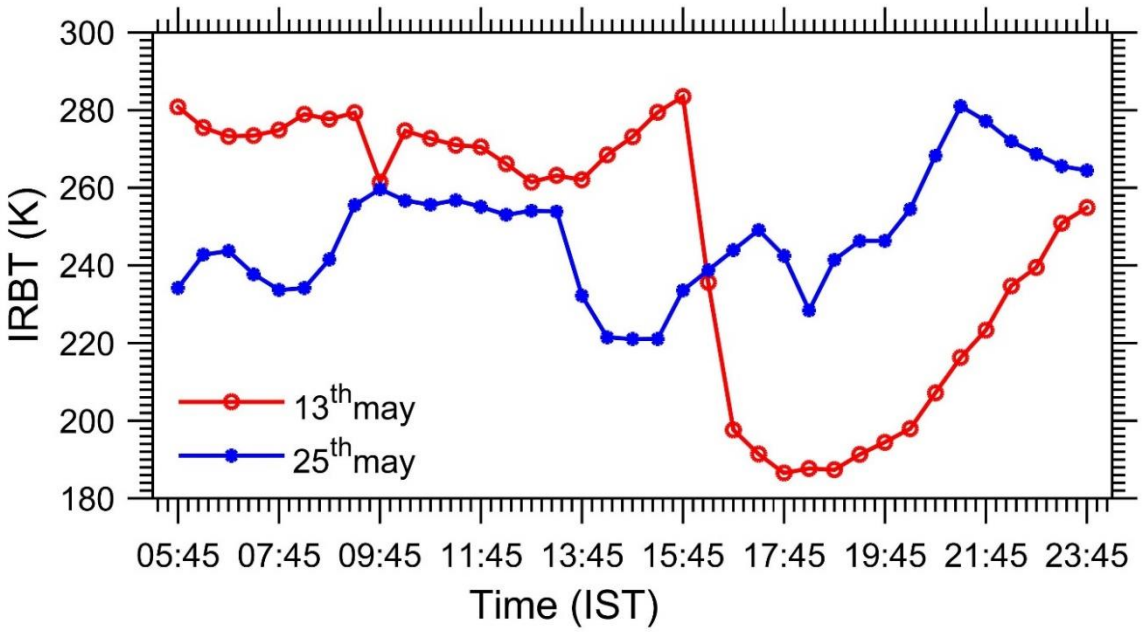

Figure 11. Time series of infrared brightness temperature (K) during the convective events on 13th May, 2018 (red) and 25th May, 2018 (blue) using INSAT-3DR satellite data.

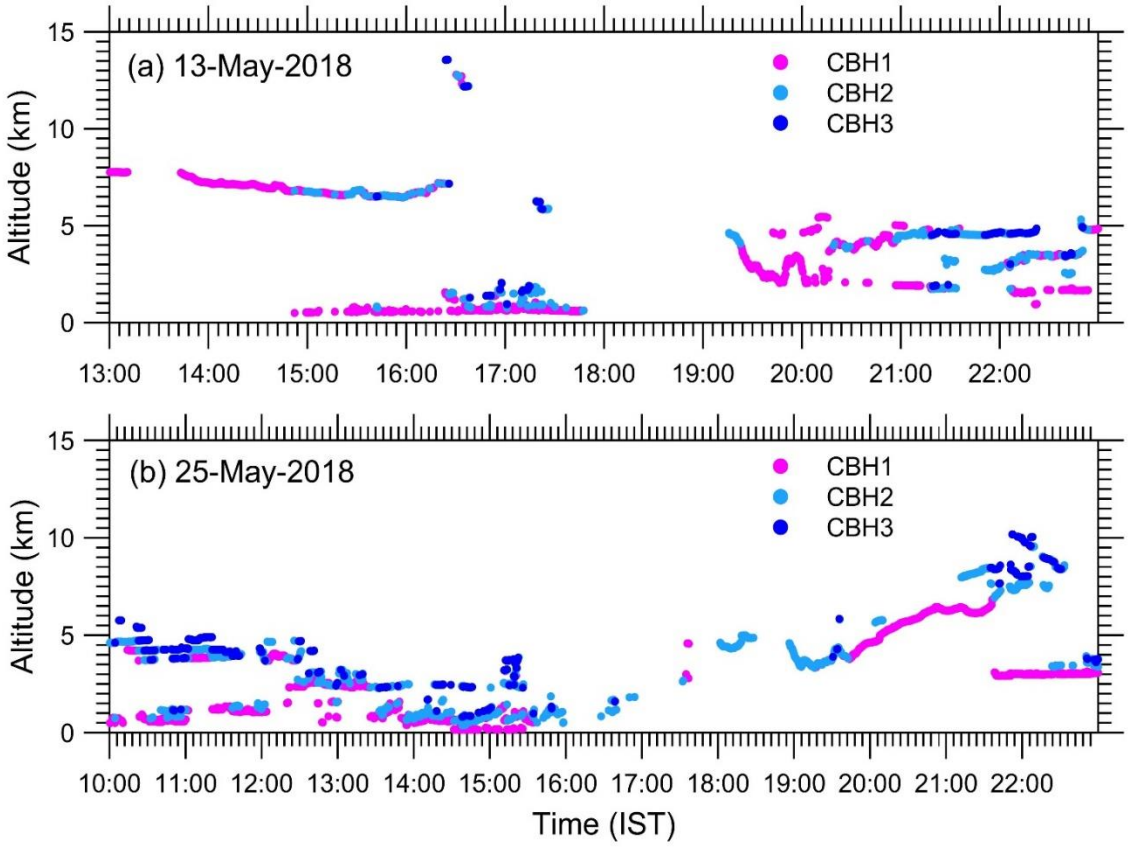

Figure 12. Time series of cloud base height (m) of layer 1 (pink), layer 2 (cyan) and layer 3 (blue) clouds during the convective events on (a) 13th May, 2018 and (b) 25th May, 2018 using ceilometer measurements at NCESS.

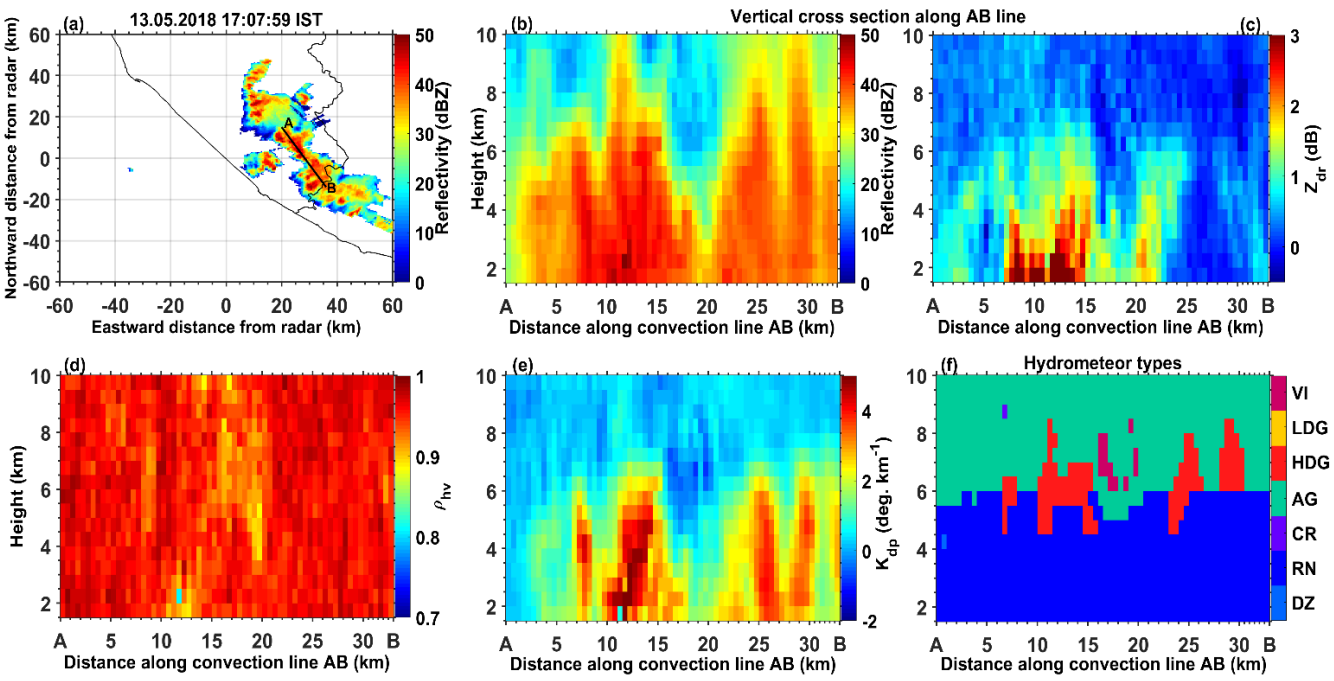

Figure 13. (a) Radar reflectivity averaged between 2.5 and 3.5 km height on 13th May, 2018. Vertical cross section of (b) reflectivity, (c) Z_{dr} , (d) ρ_{hv} , (e) K_{dp} and (f) identified hydrometeor types along AB convection line at 17:07:59 IST.

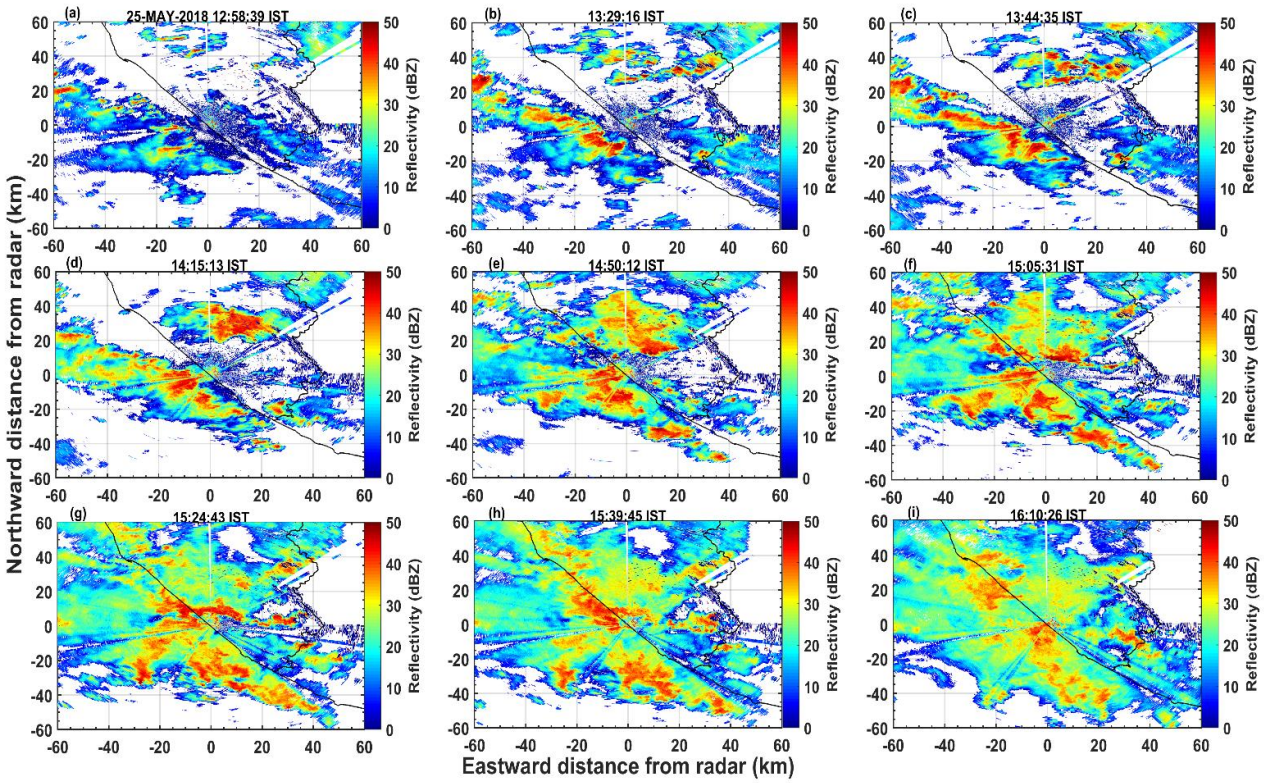

Figure 14. PPI diagrams of radar reflectivity at 2° elevation angle at 12:58:39 IST to 16:10:26 IST (a-i) during the event on 25th May, 2018.

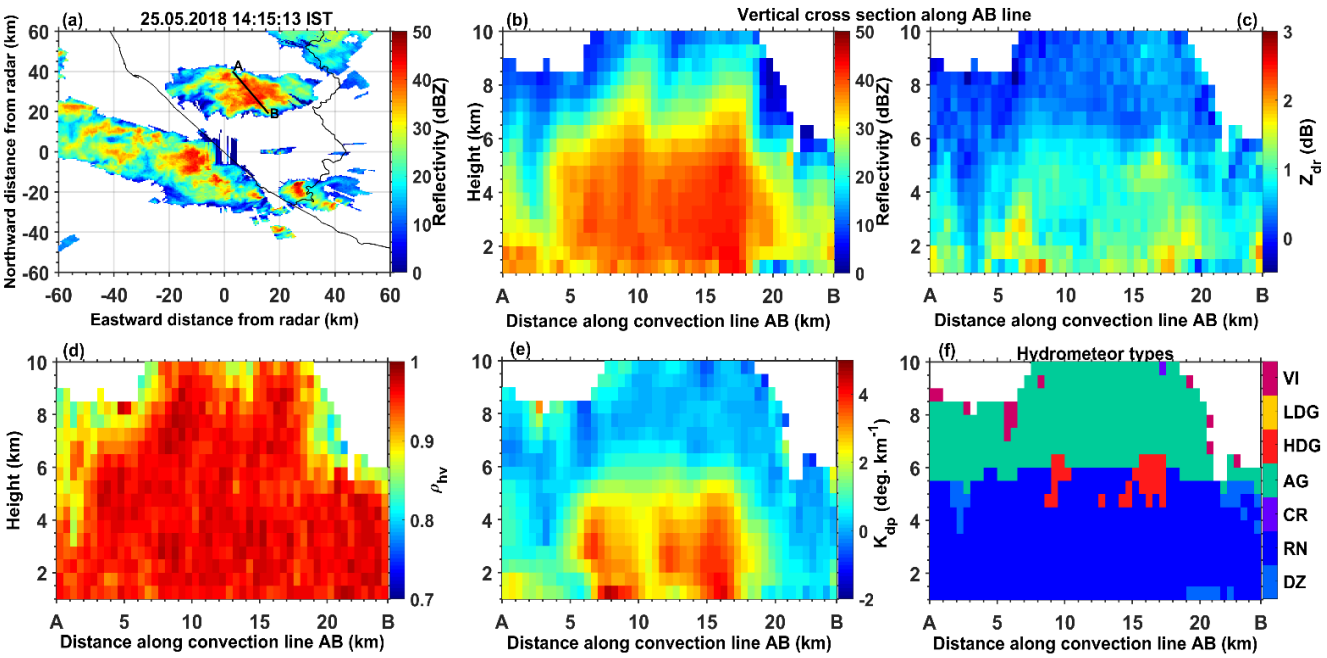

Figure 15. (a) Radar reflectivity averaged between 2.5 and 3.5 km height on 25th May, 2018. Vertical cross section of (b) reflectivity, (c) Z_{dr}, (d) ρ_{hv} , (e) K_{dp} and (f) hydrometeor types along AB convection line at 14:15:13 IST.